Advanced Pilot-in-the-Loop Control System for Aircraft Ground Handling

José Joaquín Mendoza Lopetegui, *Member, IEEE*, Lorenzo Desiderato, Giulio Loiacono, and Mara Tanelli, *Senior Member, IEEE*

***Abstract*—The high-speed regime in the aircraft rollout phase during landings is a critical stage where longitudinal and lateral stability must be maintained. In the longitudinal direction, various high-performing antiskid (AS) algorithms have been developed, aiding the pilot in minimizing the braking distance and preventing wheel locking. Instead, the lateral stability problem, which can produce runway excursions, has received considerably less attention. The presence of asymmetries, such as crosswind, runway grip variability, or failure conditions, can make the task of maintaining directional control difficult for the pilot. In this article, we propose and evaluate a modular architecture for a control system that acts as a pilot lateral assistant during ground handling maneuvers. The lateral assistant simultaneously uses commonly employed ground handling actuators to correct incipient lateral instabilities. The proposed architecture seamlessly interacts with the AS system and copes with various types of actuator failures, including the often neglected free caster dynamics from a nose wheel steering failure. The control system is evaluated in a pilot-in-the-loop simulation that accurately represents the relevant ground handling dynamics, validated using experimental data. We show that our system effectively improves directional control in various scenarios, including actuator failures and environmental disturbances that strongly excite the lateral dynamics.**

***Index Terms*—Aircraft ground handling, antiskid (AS), control allocation, landing gear, pilot-in-the-loop.**

I. INTRODUCTION

DURING landings, aircraft reach considerable speeds during the rollout phase, which makes them susceptible to stability problems both in the longitudinal and lateral directions. In particular, runway excursions are among the most commonly reported accidents, making up around 17% of all accidents reported over the last five years [1]. Human error, aircraft system faults, and poor runway conditions are among the most common causes of such accidents [2].

In the longitudinal direction, a short runway, in combination with a low runway grip, can produce runway overruns. For this reason, a highly effective antiskid (AS) system that prevents wheel locking conditions and maximizes tire–runway friction for quick deceleration is fundamental when aiming to operate at these high speeds. In recent years, significant work has been devoted to improving the longitudinal braking performance by designing effective AS algorithms. The traditional approach is for the algorithm to rely only on measuring the wheel speeds to detect and prevent incipient skids (see [3], [4]). More recent approaches aim to synthesize more performing controllers, also incorporating the information of the aircraft's longitudinal speed (see [5], [6], [7], [8]).

The strong focus in the longitudinal direction has indeed reduced the frequency of runway overrun events, and instead, lateral runway excursions have started to become a concern [9]. In the lateral direction, strong asymmetries such as runway friction variability or heavy crosswinds can deviate the aircraft's path enough to cause runway excursions. Unlike the longitudinal direction, the pilot must maintain directional stability with little help by operating the actuators that can produce yawing moments. The coupled nature of the problem between the lateral and longitudinal directions, in combination with aircraft that have unforgiving ground handling characteristics and the possibility of actuator failures during the rollout, can make the pilot's task of maintaining directional stability a considerable challenge. To tackle the problem, aircraft on-ground dynamics have been analyzed through various perspectives, typically through reduced-order models and simulation environments [10]. Very often, studies have focused on describing the influence of specific factors on directional stability, such as the impact of aerodynamic forces and velocity [11], tire inflation pressure and tire cornering stiffness [12], aircraft mass and center of gravity (CoG) position [13], [14], or shock absorber leakage [15].

To improve directional stability, most works focus on the rectification problem alone by giving complete authority to a controller. In [16], a nonlinear model-based look-ahead controller is proposed that operates exclusively on the nose wheel steering for automatic centerline tracking. In [17], a yaw-rate tracking controller based on antiwindup compensation is designed for low-speed lateral maneuvering, also using the nose wheel steering. Similar approaches are shown in [18], based on a family of local linear models, and in [19], based on feedback linearization. In [20], a combined control law for directional rectification using both the differential braking and the nose wheel steering with an optimization-based control action distribution was proposed and prototyped in a small uncrewed aerial vehicle. In [21], a model predictive controller

---

Received 29 July 2025; revised 17 October 2025; accepted 3 December 2025. Date of publication 17 December 2025; date of current version 25 February 2026. Recommended by Associate Editor M. Sato. *(Corresponding author: José Joaquín Mendoza Lopetegui.)*

José Joaquín Mendoza Lopetegui, Lorenzo Desiderato, and Mara Tanelli are with the Dipartimento di Elettronica, Informazione e Bioingegneria, Politecnico di Milano, 20133 Milan, Italy (e-mail: josejoaquin.mendoza@polimi.it; lorenzo.desiderato@polimi.it; mara.tanelli@polimi.it).

Giulio Loiacono is with the Dipartimento di Meccanica, Politecnico di Milano, 20156 Milan, Italy (e-mail: giulio.loiacono@mail.polimi.it).

Digital Object Identifier 10.1109/TCST.2025.3642909

and a linear quadratic regulator were proposed to replace pilot control through the rudder and differential braking. Closely related are works dealing with the optimal allocation of the ground handling actuators, such as [22] and [23], which also focus on actuator failures.

Instead, few works tackle the design of controllers with a pilot in the loop. Most works on the topic have attempted to introduce stability augmentation systems to aid the pilot in specific tasks. In [24], an assistance system was proposed for centerline tracking operating on differential braking. In [25], a system was proposed and evaluated to dynamically adapt the nose wheel steering response to improve the ground handling characteristics. In [26], a differential braking-based emergency system is proposed to counteract adverse yawing motions in case of nose wheel steering jamming.

As illustrated before, the currently available works have focused on alleviating the pilot's workload only partially by controlling specific actuators, mostly neglecting actuator failures, and with few considerations about proper integration with industrial-grade AS systems. To fill this gap, we develop a ground handling lateral assistance system (LAS) for pilot-in-the-loop control, exploiting all conventionally used actuators. Our main contributions are as follows.

1) The proposal and evaluation of a modular architecture supporting pilots in the high-speed rollout to maintain directional stability during centerline tracking and centerline capture using all available actuators.
2) Seamless integration with any general-purpose AS system to rectify the aircraft's direction in the face of transient lateral instabilities.
3) Dedicated attention to the often neglected but critical case of nose wheel steering failure, which degrades the control authority due to the resulting free caster dynamics.

The evaluation of the system is conducted in a MATLAB/Simulink simulation environment through the usage of a high-fidelity multibody model of a typical tricycle landing gear aircraft, validated against experimental data, already presented in [15].

The structure of this article is as follows. Section II introduces the problem, describes the dynamics involving the actuators available for ground handling, and introduces the anomalous conditions to be faced. Section III derives analytical models of the aircraft's on-ground dynamics in both the engaged and disengaged nose wheel steering cases. Section IV describes the proposed control architecture and details each subsystem. Section V presents the evaluation of the control architecture in different scenarios in a pilot-in-the-loop framework. Finally, Section VI provides some closing remarks.

II. LATERAL STABILITY PROBLEM IN AIRCRAFT GROUND HANDLING

This work is devoted to developing and evaluating a ground handling assistance system that can aid a pilot in maintaining directional control of an aircraft during the critical deceleration phase at high speeds. This section establishes the problem to be solved, the assumptions considered, and the characteristics of the aircraft that will serve as a concrete case study.

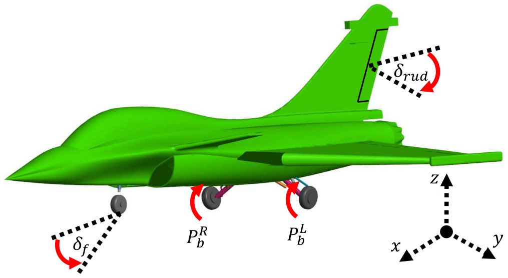

Fig. 1. Schematic view of the aircraft geometry under study in a Simscape Multibody representation. The three ground handling actuators and the aircraft's body reference frame are highlighted.

A. Problem Description

The problem under consideration is developing and evaluating an LAS that can be integrated with conventional AS systems to reduce the pilot's workload during the rollout. The system is meant to be modular and industrially useful, for which several considerations will be made regarding fault modes and practical applicability.

The aircraft type to be studied has a tricycle landing gear geometry, illustrated in Fig. 1. Its landing gear comprises the nose landing gear (NLG) and the main landing gear (MLG). The NLG corresponds to a single steerable wheel with no braking capability, while the MLG consists of two wheels with braking but no steering capabilities. For the scope of this work, it is assumed that the aircraft has already established ground contact on all its wheels. Namely, the aircraft is equipped with weight-on-wheel sensors that allow the detection of a persistent ground contact condition, which is a minimum requirement for the activation of the ground handling assistance system. The assistance system is only allowed to activate after the persistent ground contact condition has been verified for a sufficiently long time, enabling the pilot to properly complete the touchdown process, which is assumed to go smoothly. For instance, we assume that the aircraft's heading has already been straightened after a crab landing under crosswind.

B. Ground Handling Actuators Dynamics

The aircraft under consideration has three types of actuators capable of generating yawing moments to guide the aircraft's direction. Their characteristics and constraints are vastly different, adding another layer of complexity to the task. The dynamics of each relevant actuator will be described next. In the rest of the article, given the symmetry between the right and left sides of the MLG, the quantities that apply to both of its sides will have a superscript R/L for brevity of exposition. If specific focus is put on the right (or left) side, the superscript R (or L) will be used.

1) Braking Control Unit: The aircraft is endowed with a hydraulic system capable of generating independent braking pressures at each MLG side, denoted as $P_b^{R/L}$. To do so, braking

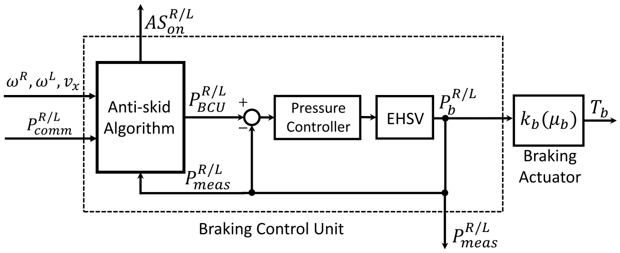

Fig. 2. Schematic view of the brake control unit and its interaction with the brake actuator. EHSV stands for electrohydraulic servo valve.

commands $P_{\text{comm}}^{R/L}$ are sent to the braking control unit (BCU). The BCU processes the command of each side of the MLG together with the rotational wheel speed information $\omega^{R/L}$ as well as the aircraft's longitudinal speed v_x, applying the final requested commands $P_{\text{BCU}}^{R/L}$ to the hydraulic system. Fig. 2 provides a schematic representation of the interaction between the BCU and the brake actuator.

For each side of the MLG, the BCU decides if the requested commands $P_{\text{comm}}^{R/L}$ are safe from the wheel rotational dynamics point of view as processed by its internal AS algorithm. The activation and deactivation conditions of the AS algorithm are as follows:

$$\begin{cases} \lambda^{R/L} > \lambda_{\text{th}} \textbf{ and } P_{\text{comm}}^{R/L} > P_{\text{AS}}^{R/L} \\ \qquad \Rightarrow P_{\text{BCU}}^{R/L} = P_{\text{AS}}^{R/L} \textbf{ and } AS_{\text{on}}^{R/L} = 1 \\ P_{\text{AS}}^{R/L} > P_{\text{comm}}^{R/L} \Rightarrow P_{\text{BCU}}^{R/L} = P_{\text{comm}}^{R/L} \textbf{ and } AS_{\text{on}}^{R/L} = 0 \end{cases} \tag{1}$$

where

$$\lambda^{R/L} = \frac{v_x - \omega^{R/L} r_w}{v_x} \tag{2}$$

in which $\lambda^{R/L}$ is the longitudinal wheel slip, r_w is the MLG tire's radius, λ_{th} is the maximum admissible slip before AS intervention, and $P_{\text{AS}}^{R/L}$ is a safe pressure command decided by the AS algorithm, designed to maximize braking performance and to prevent wheel locking. The interpretation of (1) is as follows. If the BCU deems the command unsafe due to the generation of incipient wheel skids, the AS system will override the command $P_{\text{comm}}^{R/L}$ and will apply instead its internally calculated command $P_{\text{AS}}^{R/L}$ as long as the condition $P_{\text{comm}}^{R/L} > P_{\text{AS}}^{R/L}$ is satisfied. This means, for instance, that if the pilot releases the pedals and requests a null pressure command, the AS system will always disengage.

The BCU's AS algorithm is assumed to be operated in an independent wheel configuration. Namely, the safe pressure $P_{\text{BCU}}^{R/L}$ sent to the hydraulic system is chosen based on the wheel speed information of its corresponding side only. In this work, and without loss of generality, a slip-based AS algorithm is employed, which selects $P_{\text{AS}}^{R/L}$ as the pressure required to track a slip reference $\overline{\lambda}$, aiming to maximize μ, the effective tire–runway friction. To synthesize the slip-based controller, this work uses the technique presented in [27], in which the slip-based AS algorithm design problem was treated, yielding a gain-scheduled controller with stability guarantees. It is assumed that two runway friction conditions are faced. Fig. 3 shows the assumed relationship $\mu(\lambda)$ for the two conditions considered. The two curves have been experimentally identified and defined with the support of an industrial partner.

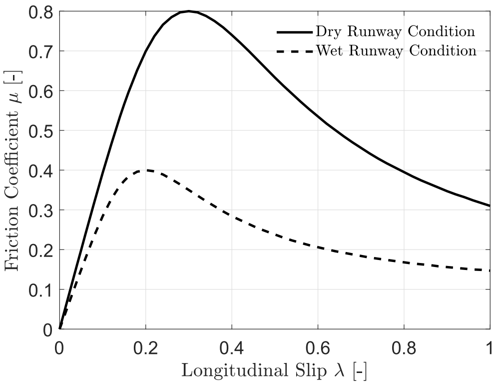

Fig. 3. Curves of the friction coefficient against the longitudinal slip for the two runway conditions taken into account.

Then, the pressure $P_{\text{BCU}}^{R/L}$ selected by the AS's algorithm acts as a reference pressure to a high-bandwidth low-level closed-loop pressure controller inside the BCU, as is common in industrial practice. It is assumed that the closed-loop response between the reference $P_{\text{BCU}}^{R/L}$ and the effectively realized pressure $P_b^{R/L}$ has been characterized and can be represented as a second-order transfer function of the form

$$P_b^{\text{CL}}(s) = \frac{e^{-s\tau_a}}{1 + 2\frac{\xi_a}{\omega_a}s + \frac{s^2}{\omega_a^2}} \tag{3}$$

where ξ_a is the damping factor, ω_a is the natural frequency, and τ_a is the actuator's delay, attributable to hydraulic and processing delays. The bandwidth of this actuator is around 20 Hz. See [28] for additional details on the modeling and dynamic identification of the brake actuator for a similar application. It shall be noted that the maximum pressure that can be applied at each side is limited by the hydraulic system's capabilities, so that $P_b^{R/L} \in [0, P_b^{\max}]$, with $P_b^{\max} > 0$ the maximum applicable pressure.

It should also be noted that since independent braking pressures can be requested for each MLG side, differential braking can be used to steer the aircraft. The auxiliary variables $\Delta P_b = P_b^L - P_b^R$, in case of the effectively realized differential pressure, and $\Delta P_{\text{comm}} = P_{\text{comm}}^L - P_{\text{comm}}^R$, in case of the requested differential pressure to the BCU will come in handy in Sections III and IV. Note ΔP_b and ΔP_{comm} need not be equal due to the possible intervention of the AS system.

Finally, making reference to Fig. 2, once a hydraulic pressure $P_b^{R/L}$ is achieved, the generated force at the end of the hydraulic line allows a set of disk brakes, consisting of rotors and stators, to come against each other. The resulting braking torque is denoted as T_b and can be found as $T_b^{R/L} = k_b(\mu_b)P_b^{R/L}$, with $k_b(\mu_b)$ a conversion coefficient that depends on the brake pads' friction coefficient μ_b. The conversion coefficient depends on geometrical and physical construction factors as well as the wear condition of the brakes. In this work, we use the methods developed in [28], where the dynamics of the conversion coefficient were analyzed and characterized for a similar application.

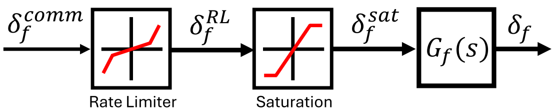

Fig. 4. Schematic of the steering system dynamics.

2) Steering Control Unit: The steering control unit (SCU) realizes a steering angle δ_f at the NLG from a commanded angle δ_f^{comm}. The dynamics of the steering system are represented in Fig. 4.

To ensure that the effectively realized steering angle δ_f closely follows the commanded angle δ_f^{comm}, a low-level closed-loop servo controller is in place. To guarantee that the low-level controller keeps the commanded angle within admissible bounds and remains within specifications, the commanded angle δ_f^{comm} is first rate limited to compute δ_f^{RL} and then saturated to compute δ_f^{sat}. Therefore, the previous variables obey the constraints $\dot{\delta}_f^{\mathrm{RL}} \in [-\dot{\delta}_f^{\max}, \dot{\delta}_f^{\max}]$ and $\delta_f^{\mathrm{sat}} \in [-\delta_f^{\max}, \delta_f^{\max}]$, where $\dot{\delta}_f^{\max} > 0$ and $\delta_f^{\max} > 0$ are the symmetric rate and position limits, respectively.

Next, the processed command δ_f^{sat} is passed to the low-level controller. The controller's closed-loop response between the requested command δ_f^{sat} and the effectively realized steering angle δ_f can be represented by a second-order transfer function of the form

$$G_f(s) = \frac{1 + s\tau_f}{\left(1 + sT_{1f}\right)\left(1 + sT_{2f}\right)} \tag{4}$$

where τ_f, T_{1f}, and T_{2f} are the time constants of the involved zero and poles. The bandwidth of this actuator is around 2 Hz.

3) Rudder Control Unit: The rudder control unit (RCU) realizes an effective rudder deflection angle δ_{rud} from a commanded angle $\delta_{\mathrm{rud}}^{\mathrm{comm}}$. The command $\delta_{\mathrm{rud}}^{\mathrm{comm}}$ is first saturated between the allowable physical limits of the rudder control surface so that the intermediate variable $\delta_{\mathrm{rud}}^{\mathrm{sat}}$ is calculated, which obeys $\delta_{\mathrm{rud}}^{\mathrm{sat}} \in [-\delta_{\mathrm{rud}}^{\max}, \delta_{\mathrm{rud}}^{\max}]$, with $\delta_{\mathrm{rud}}^{\max} > 0$ the saturation limit of the rudder's deflection. Then, a low-level closed-loop servo controller is in place so that the effectively realized rudder deflection angle δ_{rud} tracks the processed rudder deflection command $\delta_{\mathrm{rud}}^{\mathrm{sat}}$. The servo loop's closed-loop response can be represented by a third-order transfer function of the form

$$G_{\mathrm{rud}}(s) = \frac{1}{1 + 2\frac{\xi_{\mathrm{rud}}}{\omega_{\mathrm{rud}}}s + \frac{s^2}{\omega_{\mathrm{rud}}^2}} \frac{1}{1 + T_{\mathrm{rud}}s} \tag{5}$$

where ξ_{rud} and ω_{rud} are the damping factor and natural frequency associated with the pair of complex conjugate poles, while T_{rud} is the time constant of the residual dynamics. The bandwidth of this actuator is around 10 Hz.

C. Anomalous Conditions

The previously described ground handling actuators can be subject to failures during the aircraft's operation. Different kinds of failures can alter the aircraft's on-ground dynamics differently, which calls for a robust LAS. Since, in practice, the fault modes that such a system can sustain are vast, a representative set of failures is considered in this work. It is assumed that each of the three actuators can sustain a specific failure at any moment during the ground handling maneuver, and simultaneous failures are allowed.

It is considered that the BCU can indicate its health status by a binary variable denoted as $\mathrm{HS}_{\mathrm{BCU}}$. It is assumed that the aircraft is equipped with redundant electronic and hydraulic systems, allowing the BCU to reconfigure in the event of a failure. Therefore, in case $\mathrm{HS}_{\mathrm{BCU}} = 0$, which indicates a BCU component failure, the pressure commands $P_{\mathrm{comm}}^{R/L}$ are ignored, and the BCU receives a null command during the period of time while the backup unit enters operation. After the backup unit is operative, $\mathrm{HS}_{\mathrm{BCU}} = 1$, and the brake commands $P_{\mathrm{comm}}^{R/L}$ are processed again. In practice, due to the low chance that both the main unit and the backup unit fail simultaneously, this work considers only a transient failure of the main unit for the BCU per braking maneuver so that the braking authority will eventually recover after a failure.

The SCU can also indicate its health status by a binary variable denoted as $\mathrm{HS}_{\mathrm{SCU}}$. In case $\mathrm{HS}_{\mathrm{SCU}} = 0$, which indicates an SCU failure, the SCU is unable to impose the steering angle δ_f, and the measurement of this signal becomes unavailable. Instead, the steering system defaults to a disengaged steering configuration, in which δ_f evolves in a free caster condition. Section III-B will provide more details about the disengaged steering mode configuration. Once this type of failure occurs, it remains in place until the completion of the braking maneuver.

Finally, the RCU can also indicate its health status by a binary variable denoted as $\mathrm{HS}_{\mathrm{RCU}}$. In case $\mathrm{HS}_{\mathrm{RCU}} = 0$, which indicates an RCU failure, the rudder becomes jammed and maintains its last position before the failure, and the rudder command $\delta_{\mathrm{rud}}^{\mathrm{comm}}$ becomes ineffective. Once this type of failure occurs, it remains in place until the completion of the braking maneuver.

III. REDUCED-ORDER MODELING OF THE GROUND HANDLING DYNAMICS

An analytical representation of the main dynamics of interest of the aircraft during on-ground motion will be instrumental in designing the ground handling LAS. As stated in Section II, the modeling concerns the aircraft's dynamics after establishing firm ground contact. In this section, two operating modes will be described, each one associated with the engagement status of the SCU. This will allow the LAS to reconfigure if a steering failure is detected. Note that the models developed in this section are intended as control-oriented models amenable to control system design; as such, they intentionally aim to capture only the most essential elements of the ground handling dynamics. In Section V instead, the LAS is evaluated in a significantly more complex ground handling simulator validated using real flight data from an industrial partner. The models developed in this section assume planar dynamics, neglecting the pitching and rolling motions and the vertical suspension dynamics. Moreover, the modeling will concern the main aircraft body dynamics after the ground handling actuators' dynamics. Namely, we will deal with variables δ_f, $P_b^{R/L}$, and δ_{rud} instead of δ_f^{comm}, $P_{\mathrm{comm}}^{R/L}$, and $\delta_{\mathrm{rud}}^{\mathrm{comm}}$.

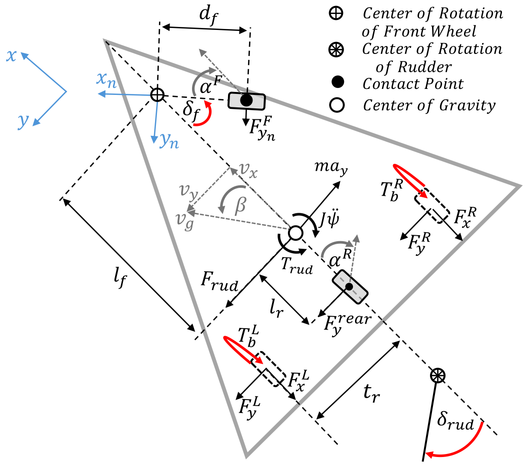

Fig. 5. Graphical representation of the bicycle model with forces and moments acting on the system, represented by solid arrows. The velocities of relevant points are represented instead by dashed arrows. Highlighted in red are the inputs by the ground handling actuators. Highlighted in blue are the aircraft's main body reference frame (x, y) and the nose wheel's reference frame (x_n, y_n).

A. Engaged Steering Dynamics

A schematic representation of the main variables involved in the ground handling dynamics is shown in Fig. 5. As shown in Fig. 5, the scheme represents the aircraft negotiating a generic curve while braking. The positive displacement of all actuators has been defined so that a positive rotation around the Z-axis is generated. Two reference frames are defined: the aircraft's main body reference frame (x, y) and the nose wheel's reference frame (x_n, y_n). Subscripts x and y are used to refer to quantities aligned with axes x and y, whereas subscripts x_n and y_n are used to refer to quantities aligned with axes x_n and y_n. In Fig. 5, the aircraft has a ground speed of v_g, with a corresponding side-slip angle of β, and associated longitudinal and lateral velocities of v_x and v_y, respectively. The aircraft has a total mass m and a rotational inertia J around the Z-axis with respect to its CoG. The lateral acceleration is denoted as a_y, whereas the yaw acceleration is denoted as $\ddot{\psi}$. The distance between the connection point of the nose wheel to the aircraft's fuselage and the aircraft's CoG is denoted as l_f, whereas the distance between the CoG and the centers of the rear wheels is named as l_r. Instead, the lateral distance between the aircraft's longitudinal axis and each MLG wheel's longitudinal axis is named as t_r. The longitudinal and lateral forces generated at the contact patch of the MLG's tires are denoted as $F_x^{R/L}$ and $F_y^{R/L}$, respectively. Since the nose wheel has no braking capability, it is assumed that negligible longitudinal force is provided by its tire, so that only the lateral force $F_{y_n}^F$ is considered, with an associated side-slip angle α^F. As can be appreciated, the nose wheel's vertical axis is off-center with respect to its connection point to the fuselage, and the associated mechanical trail is denoted as d_f. The rudder's deflection generates an equivalent force F_{rud} and moment T_{rud} referred to the CoG. Note also that for modeling purposes, a bicycle model geometry is adopted so that a fictitious tire aligned with the aircraft's longitudinal axis is considered, with an equivalent lateral force F_y^{rear} and side-slip angle α^R.

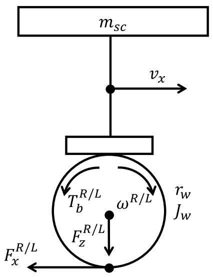

Fig. 6. Single-corner model representing the longitudinal dynamics at the wheel level of the MLG.

After a force balance along the lateral axis and a moment balance along the vertical axis, the following system of equations is obtained:

$$
\begin{aligned}
ma_y - F_{\text{rud}} - F_y^{\text{rear}} - F_{y_n}^F \cos\left(\delta_f\right) &= 0\\
J\ddot{\psi} + F_y^{\text{rear}} l_r - F_{y_n}^F \left(l_f \cos\left(\delta_f\right) - d_f\right)&\\
- T_{\text{rud}} - t_r\left(F_x^L - F_x^R\right) &= 0
\end{aligned}
\tag{6}
$$

where $F_y^{\text{rear}} = F_y^L + F_y^R$. A linear form of system (6) will now be sought, as it will be useful for control system design. Consider that the lateral tire–runway contact forces can be written in the form $F_y^{\text{rear}} = C_y^R \alpha^R$ and $F_{y_n}^F = C_y^F \alpha^F$, with C_y^R and C_y^F the rear and front cornering stiffness of the MLG and NLG tires, respectively. Next, if a small-angle approximation is used on angles β, δ_f, α^R, and α^F, and neglecting second-order terms, the following kinematic relationships can be established:

$$
\alpha^R = -\beta + \frac{l_r\dot{\psi}}{v_g}, \quad \alpha^F = \delta_f - \beta + \frac{d_f\dot{\delta}_f - l_f\dot{\psi}}{v_g}. \tag{7}
$$

The force F_{rud} and the moment T_{rud} generated by the rudder and referred to the CoG are nonlinear functions of the aircraft's side-slip angle, the aircraft's angle of attack, and the rudder deflection. Due to the planar motion assumption, the angle of attack is considered null. Then, to obtain tractable expressions, the angles β and δ_{rud} are considered small, so that

$$
\begin{aligned}
F_{\text{rud}} &= \frac{1}{2}\rho v_a^2 S \left(C_\beta^F \beta + C_{\text{rud}}^F \delta_{\text{rud}}\right)\\
T_{\text{rud}} &= \frac{1}{2}\rho v_a^2 S\, b \left(C_\beta^T \beta + C_{\text{rud}}^T \delta_{\text{rud}}\right)
\end{aligned}
\tag{8}
$$

where ρ is the air mass density, S is a reference surface, b is the wingspan, v_a is the modulus of the relative velocity vector of the aircraft with respect to the surrounding air, whereas C_β^F, C_β^T, C_{rud}^F, and C_{rud}^T are the linear sensitivities of F_{rud} and T_{rud} with respect to β and δ_{rud}.

Next, to represent the longitudinal forces F_x^L and F_x^R in a convenient way, we use the single-corner representation of the wheel dynamics of the MLG. Fig. 6 represents the relevant portion of the dynamics of interest at the MLG wheel level. In Fig. 6, m_{sc} represents the portion of the aircraft's mass sustained by one MLG wheel, r_w refers to the wheel's radius, J_w is the wheel's inertia including all contributions by the braking system, and $F_z^{R/L}$ is the effective load at the tire's contact patch. The result of a moment balance around each wheel center point yields

$$J_w\dot{\omega}^{R/L} + T_b^{R/L} - F_x^{R/L} r_w = 0. \tag{9}$$

Since the wheel dynamics are significantly faster than the longitudinal aircraft dynamics, we can consider v_x constant and avoid dealing with the deceleration dynamics. Consider next that the longitudinal tire–runway contact forces can be written in the form $F_x^{R/L} = C_x\lambda^{R/L}$, with C_x the longitudinal stiffness of the MLG tires. Note that the AS system will enforce the previous assumption, which prevents excursions of the slip dynamics into the backside of the friction curve. Using the previous assumptions together with the definition of the longitudinal slip in (2) and the wheel rotational dynamics in (9), we obtain

$$\dot{\lambda}^{R/L} = -\frac{C_x r_w^2}{J_w v_x}\lambda^{R/L} + \frac{\overline{k_b} r_w}{J_w v_x} P_b^{R/L} \tag{10}$$

where $\overline{k_b}$ is the average conversion coefficient of the brakes over their operational life.

Combining (6)–(8) and (10), and assuming slowly varying v_g with respect to the lateral dynamics, we obtain

$$\begin{aligned}
\dot{\beta} &= \frac{\rho v_a^2 S\left(C_\beta^F\beta + C_{\text{rud}}^F\delta_{\text{rud}}\right)}{2mv_g} + \frac{C_y^R}{mv_g}\left(-\beta + \frac{l_r\dot{\psi}}{v_g}\right) - \dot{\psi}\\
&\quad + \frac{C_y^F}{mv_g}\left(\delta_f - \beta + \frac{d_f\dot{\delta}_f - l_f\dot{\psi}}{v_g}\right)\\
J\ddot{\psi} &= \frac{1}{2}\rho v_a^2 S b\left(C_\beta^T\beta + C_{\text{rud}}^T\delta_{\text{rud}}\right) - C_y^R l_r\left(-\beta + \frac{l_r\dot{\psi}}{v_g}\right)\\
&\quad + C_y^F\left(l_f - d_f\right)\left(\delta_f - \beta + \frac{d_f\dot{\delta}_f - l_f\dot{\psi}}{v_g}\right) + C_x t_r\Delta\lambda\\
\Delta\dot{\lambda} &= -\frac{C_x r_w^2}{J_w v_x}\Delta\lambda + \frac{\overline{k_b} r_w}{J_w v_x}\Delta P_b
\end{aligned} \tag{11}$$

where $\Delta\lambda = \lambda^L - \lambda^R$. We assume next a small factor $d_f\dot{\delta}_f$ due to the rate limitation constraint from Section II-B2 together with a small value of d_f. We also consider that the slip dynamics of $\Delta\lambda$ in response to a differential pressure ΔP_b are much faster with respect to the lateral aircraft dynamics, which means that a static relationship between $\Delta\lambda$ and ΔP_b can be recovered. The corresponding linearized dynamics can be expressed by the following state space system:

$$\begin{bmatrix}\dot{\beta} & \ddot{\psi}\end{bmatrix}^T = A_e\begin{bmatrix}\beta & \dot{\psi}\end{bmatrix}^T + B_e\begin{bmatrix}\Delta P_b & \delta_f & \delta_{\text{rud}}\end{bmatrix}^T \tag{12}$$

where matrices A_e and B_e are reported in (13), as shown at the bottom of the page. System (12) allows the expression of the relevant lateral quantities of the problem in a form useful for the control system design undertaken in Section IV. Note that both A_e and B_e are dependent on the velocities v_a and v_g, which leads to time-varying coefficients.

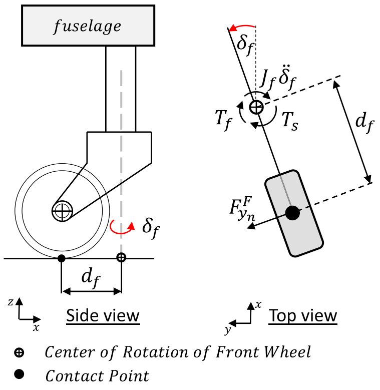

Fig. 7. Graphical representation of the disengaged steering geometry, forces, and moments involved.

B. Disengaged Steering Dynamics

As indicated in Section II-C, when the SCU suffers a failure, the closed-loop controller at the SCU is unable to impose a steering angle δ_f. Fig. 7 shows a graphical representation of the geometry of the nose wheel steering joint during the disengaged steering regime. As can be appreciated, the steering joint has a rotational inertia J_f referred to the center of rotation of the front wheel. It interacts with the runway through the lateral force $F_{y_n}^F$ at the contact patch and the self-aligning moment T_s. The moment T_f refers to the friction torque that resists rotation due to the friction at the steering column.

The associated moment balance reads

$$J_f\ddot{\delta}_f = -T_s - T_f - F_{y_n}^F d_f. \tag{14}$$

In this work, we use the Fiala model [29] to represent the self-aligning moment, which takes the form

$$T_s = \begin{cases} 2\left|F_z^F\right| w_f\mu_y^F\left(1-H\right)H^3\,\text{sign}\left(\alpha^F\right), & \text{if } \left|\alpha^F\right| \le \alpha_c\\ 0, & \text{if } \left|\alpha^F\right| > \alpha_c\end{cases} \tag{15}$$

where F_z^F is the vertical force on the NLG tire's contact patch, w_f is the NLG tire's width, μ_y^F is the lateral friction coefficient between the tire and runway, α^F is the NLG tire's side-slip angle, α_c is a critical slip value separating the stages of elastic tire deformation ($|\alpha^F| \le \alpha_c$) and complete tire sliding ($|\alpha^F| > \alpha_c$), and H is an auxiliary variable computed as follows:

$$H = 1 - \frac{C_y^F\left|\tan\left(\alpha^F\right)\right|}{3\mu_f^F\left|F_z^F\right|}. \tag{16}$$

$$A_e = \begin{bmatrix} \dfrac{\rho v_a^2 S C_\beta^F}{2mv_g} - \dfrac{C_y^R + C_y^F}{mv_g} & \dfrac{C_y^R l_r - C_y^F l_f}{mv_g^2} - 1\\ \dfrac{\rho v_a^2 S bC_\beta^T}{2J} + \dfrac{C_y^R l_r - C_y^F\left(l_f - d_f\right)}{J} & -\dfrac{C_y^R l_r^2 + C_y^F\left(l_f - d_f\right)l_f}{Jv_g}\end{bmatrix} \quad B_e = \begin{bmatrix} 0 & \dfrac{C_y^F}{mv_g} & \dfrac{\rho v_a^2 S C_{\text{rud}}^F}{2mv_g}\\ \dfrac{\overline{k_b} t_r}{J r_w} & \dfrac{C_y^F\left(l_f - d_f\right)}{J} & \dfrac{\rho v_a^2 S bC_{\text{rud}}^T}{2J}\end{bmatrix} \tag{13}$$

Instead, we consider the friction torque to be described as indicated by the steering column's manufacturer, which takes the form

$$T_f = \overline{T_f}\,\mathrm{sign}\left(\dot{\delta}_f\right) \tag{17}$$

where $\overline{T_f}$ refers to a constant quantifying the magnitude of the friction torque.

Similarly, as done in Section III-A, we seek a control-oriented representation of the dynamics in this steering mode. We will consider a small side-slip angle α^F, which implies that only the elastic deformation stage needs to be considered in (15). By replacing (16) in (15), using a small angle approximation for α^F, and neglecting higher order terms, we obtain

$$T_s = \frac{2w_f C_y^F \alpha^F}{3}. \tag{18}$$

Instead, (17) does not immediately admit a clean linear approximation. To avoid neglecting this term, we use the approximation

$$T_f = \gamma \dot{\delta}_f \tag{19}$$

where γ is a constant parameter that can be chosen to shape the approximation. Higher values of γ will yield better approximations near $\dot{\delta}_f = 0$ but will overestimate this effect for high steering rates. In this work, we select $\gamma = 2\overline{T_f}/\dot{\delta}_f^{\max}$, which can be interpreted as the linear slope needed to make the nonlinearity coincide with the linear approximation at half of the rate-limited steering rate $\dot{\delta}_f$. Therefore, combining (14), (18), and (19), the kinematic relationship for α^F from (7), and augmenting system (11) with the disengaged steering dynamics, we can write the linearized state space system as follows:

$$\begin{aligned}\left[\dot{\beta} \quad \ddot{\psi} \quad \dot{\delta}_f \quad \ddot{\delta}_f\right]^T &= A_d \left[\beta \quad \dot{\psi} \quad \delta_f \quad \dot{\delta}_f\right]^T \\ &\quad + B_d \left[\Delta P_b \quad \delta_{\mathrm{rud}}\right]^T \end{aligned} \tag{20}$$

where matrices A_d and B_d are defined as follows:

$$A_d = \begin{bmatrix} A_e^{11} & A_e^{12} & B_e^{12} & \dfrac{C_y^F d_f}{m v_g^2} \\ A_e^{21} & A_e^{22} & B_e^{22} & \dfrac{C_y^F \left(l_f - d_f\right) d_f}{J v_g} \\ 0 & 0 & 0 & 1 \\ \dfrac{\Omega_f}{J_f} & \dfrac{\Omega_f l_f}{J_f v_g} & -\dfrac{\Omega_f}{J_f} & -\dfrac{1}{J_f}\left(\gamma + \dfrac{\Omega_f d_f}{v_g}\right) \end{bmatrix}$$

$$B_d = \begin{bmatrix} 0 & B_e^{13} \\ B_e^{21} & B_e^{23} \\ 0 & 0 \\ 0 & 0 \end{bmatrix}. \tag{21}$$

In (21), reference is made to some elements of matrices A_e and B_e in (13) for a more compact representation. Moreover, the auxiliary variable Ω_f is used, defined as follows:

$$\Omega_f = C_y^F \left(d_f + \frac{2w_f}{3}\right). \tag{22}$$

Note that in system (21), we do not assume a small factor $d_f \dot{\delta}_f$ anymore, as the rate limit constraint on $\dot{\delta}_f$ normally imposed by the controller becomes disconnected in this operating mode.

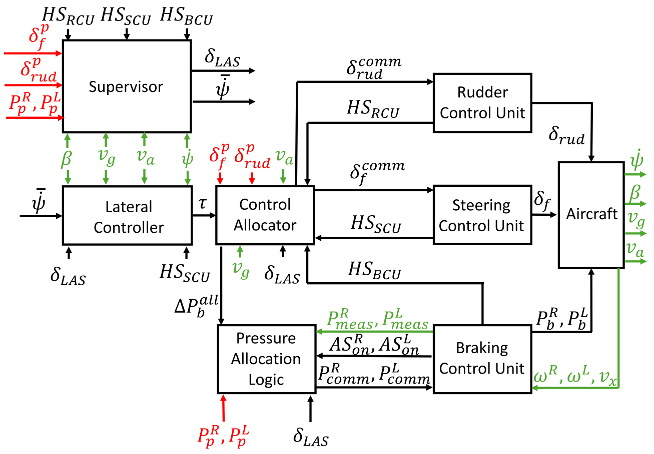

Fig. 8. Architecture of the ground handling LAS. The signals in red are the requests to the ground handling actuators coming from the pilot. The signals in green are measurements from the aircraft. The signals in black are internal.

IV. Control System Proposal

This section presents our proposal for the LAS to handle the dynamics described in Sections II and III. We start by presenting the proposed architecture of the system and then continue with the description of each block comprising the architecture.

A. Control System Architecture

The architecture of the LAS is presented in Fig. 8.

The architecture proposed is modular so that each block can be adapted to satisfy different system requirements. It processes the pilot input requests in terms of nose wheel steering δ_f^p, rudder deflection δ_{rud}^p, and pressures P_p^R and P_p^L that are commanded to each side of the MLG. Depending on the state of the aircraft, quantified through the ground speed v_g, the airspeed v_a, the side-slip angle β, the yaw rate $\dot{\psi}$, and the actuator health status signals $\mathrm{HS}_{\mathrm{RCU}}$, $\mathrm{HS}_{\mathrm{SCU}}$, and $\mathrm{HS}_{\mathrm{BCU}}$, the LAS evaluates whether the pilot's inputs require adjustment or not, indicated by the variable $\delta_{\mathrm{LAS}} \in \{0, 1\}$. If no adjustment is necessary, $\delta_{\mathrm{LAS}} = 0$, and the pilot inputs are directly passed to the control units of the actuators. In case adjustment is necessary, $\delta_{\mathrm{LAS}} = 1$, and this binary variable is propagated internally to activate the different modules to solve the transient lateral instability. To do that, a reference yaw rate $\bar{\dot{\psi}}$ is computed and tracked to aid the pilot in returning the aircraft to a controllable condition. The required adjustment is quantified using a virtual input τ representing the moment around the vertical axis at the CoG that should be injected into the aircraft. The virtual input τ is realized through a control allocator that requests a rudder deflection $\delta_{\mathrm{rud}}^{\mathrm{comm}}$, a nose wheel steering angle δ_f^{comm}, and a differential pressure $\Delta P_b^{\mathrm{all}}$. Due to the interaction between the requested differential pressure and the AS system, a Pressure Allocation Logic module is necessary to generate the appropriate pressure commands P_{comm}^R and P_{comm}^L requested by the BCU, which depend on the activation status of each side of the AS $\mathrm{AS}_{\mathrm{on}}^{R/L}$, the measured pressures P_{meas}^R and P_{meas}^L, as well as the pilot requests.

Remark 1: The focus of the control system described in this section will be assisting the pilot in mitigating directional problems during the rollout phase after landing. However, the architecture presented in Fig. 8 can also accommodate the takeoff acceleration phase by suitably adapting the control system's parameters, such as the range of admissible speeds in which the LAS is allowed to trigger, and taking into account that braking actions are expected to be seldom used during takeoff.

In Sections IV-B–IV-E, the different modules comprising the architecture will be described, together with their design considerations.

B. Supervisor Module

The Supervisor module interfaces with the pilot and the LAS. It processes the pilot requests and the aircraft states to decide if command corrections are necessary. Command corrections are only computed if $v_g > v_g^{\text{th}}$, with v_g^{th} a threshold that ensures that the LAS will not interfere with low-speed, low-risk ground handling tasks that might request strong lateral motion, typically encountered during taxiing before takeoff. Moreover, $\delta_{\text{LAS}} = 0$ as long as the aircraft's yaw rate $\dot{\psi}$ remains inside a yaw rate envelope deemed adequate. The maximum admissible limit before triggering the assistance system for the yaw rate in absolute value is denoted as $\dot{\psi}_{\text{th}}$, which is a dynamic threshold computed as follows:

$$\dot{\psi}_{\text{th}} = \dot{\psi}_{\text{th}}^{\min} + \frac{\alpha_{\text{th}}}{\sqrt{v_g}} + \beta_{\text{th}} v_g \left(\frac{C_y^F \left(-\beta + \delta_f\right) - C_y^R \beta}{m v_g^2 - C_y^R l_r + C_y^F l_f} \right) + \frac{\beta_{\text{th}} v_g}{2} \left(\frac{\rho v_a^2 S \left(C_\beta^F \beta + C_{\text{rud}}^F \delta_{\text{rud}} \right)}{m v_g^2 - C_y^R l_r + C_y^F l_f} \right) \tag{23}$$

where $\alpha_{\text{th}} > 0$ and $\beta_{\text{th}} > 0$ are weighting parameters, whereas $\dot{\psi}_{\text{th}}^{\min}$ is a constant threshold parameter. In (23), $\dot{\psi}_{\text{th}}^{\min}$ represents the minimum yaw rate acceptable, below which no command correction will take place. The term proportional to α_{th} accounts for the speed variability inside the operational envelope since higher yaw rate excursions are typically admissible at lower speeds. To account for such a relationship, an inversely proportional factor to v_g is proposed. In particular, we choose a factor of $1/\sqrt{v_g}$ to shape the inverse relationship as a heuristic based on the flight data available for the tuning of the threshold. Instead, the term proportional to β_{th} accounts for the expected yaw rate generated by a steering angle δ_f and a rudder deflection δ_{rud} during constant velocity cornering conditions. In particular, the term can be recovered by taking the first equation of system (11) and considering that an admissible gentle lateral request would employ mild steering and rudder deflection values. This implies that the side-slip angle rate $\dot{\beta}$ and steering rate $\dot{\delta}_f$ contributions can be neglected, allowing us to solve for the expected yaw rate.

The tuning of α_{th}, β_{th}, and $\dot{\psi}_{\text{th}}^{\min}$ has been made using offline data and later refined during pilot-in-the-loop testing. More specifically, experimental flight test data were provided by the industrial partner, which contained maneuvers rated both positively and negatively by pilots during taxiing and landing at different speeds, encompassing the operational envelope while trying to accomplish tasks such as centerline capture and centerline tracking. The rating scale used was the Cooper–Harper scale [30], which quantifies the workload required by the pilot to accomplish the task. The parameters in (23) were chosen so that a rating above 5 would have triggered the LAS in all evaluated maneuvers, while a rating of 5 or below would not have done so. Note that since the assistance system triggers once the threshold $\dot{\psi}_{\text{th}}$ is exceeded, parameters α_{th}, β_{th}, and $\dot{\psi}_{\text{th}}^{\min}$ should also be selected leaving some margin with respect to the absolute maximum acceptable yaw rate values, since the assistance system requires some time to inject the yaw moment and correct the directional instability.

If $|\dot{\psi}(t)| > \dot{\psi}_{\text{th}}(t)$ is satisfied at time t, $\delta_{\text{LAS}} = 1$ and a reference yaw rate $\bar{\dot{\psi}}$ is computed. The reference yaw rate is selected as $\bar{\dot{\psi}} = (\dot{\psi}_{\text{th}}(t) - \epsilon_{\text{th}})\,\text{sign}\,(\dot{\psi}(t))$ and is kept constant until the transient instability is solved, with $\epsilon_{\text{th}} > 0$ a small yaw rate margin to ensure the reference is sufficiently inside the yaw rate envelope. Therefore, the reference is selected as an admissible yaw rate inside the envelope that still turns the aircraft in the intended direction of motion. During pilot-in-the-loop evaluation, the previous choice has been overwhelmingly preferred over alternatives such as setting $\bar{\dot{\psi}} = 0$, which tend to interfere with the pilot's intention even if the reference is well within the envelope.

Once the LAS starts tracking the reference $\bar{\dot{\psi}}$, a handover strategy is needed to declare when the correction commands should cease, and the control authority returned to the pilot. To do so, it is necessary to check that the lateral instability has been solved and that the pilot's commands are safe and consistent with the current aircraft's motion for a smooth handover. Therefore, the pilot's inputs δ_f^p, δ_{rud}^p, P_p^L, and P_p^R need to be processed to infer the pilot's intention. The pilot's intention inference is computed as follows;

$$\dot{\psi}_p = \begin{cases} \left(-A_e^{-1} B_e \begin{bmatrix} \Delta P_b^p & \delta_f^p & \delta_{\text{rud}}^p \end{bmatrix}^T \right)_2, & \text{if } HS_{\text{SCU}} = 1 \\ \left(-A_d^{-1} B_d \begin{bmatrix} \Delta P_b^p & \delta_{\text{rud}}^p \end{bmatrix}^T \right)_2, & \text{if } HS_{\text{SCU}} = 0 \end{cases} \tag{24}$$

where $\dot{\psi}_p$ is an estimation of the pilot's intention in the form of a desired yaw rate, $\Delta P_b^p = P_p^L - P_p^R$, the notation $(\cdot)_2$ indicates that the second entry of the vector inside parenthesis is extracted, whereas A_e^{-1} and A_d^{-1} are the inverse matrices of (13) and (21), respectively. Expression $\dot{\psi}_p$ is the yaw rate component of the steady-state solution of (12) and (20). From a practical implementation point of view, the matrices A_e and A_d are always invertible inside the operational envelope of the case study. However, monitoring their condition numbers and adjusting the inversion's method accuracy at low speeds is advisable due to the influence of v_g in some of their entries. The pilot's intention inference method has been proposed as a simple heuristic that allows directly linking the measurable pilot commands with a steering rate value coherent with the aircraft's dynamics. Potentially, more in-depth models of the pilot's internal dynamics could be employed for a more accurate estimation, which can be implemented with minor modifications to (24) due to the modular nature of the LAS.

Once $\dot{\psi}_p$ is obtained, the handover is managed as follows:

$$\delta_{\mathrm{LAS}} = \begin{cases} 0, & \text{if } \dot{\psi}_p \,\mathrm{sign}\left(\overline{\dot{\psi}}\right) < \left|\overline{\dot{\psi}}\right| \textbf{ and } T_{\mathrm{th}} = 1 \\ 1, & \text{otherwise} \end{cases} \tag{25}$$

where T_{th} is a binary variable that takes a value of 1 if the yaw rate $\dot{\psi}$ has remained inside the admissible envelope for a time T. Therefore, time T should be interpreted as a persistence time. The intended effect behind the handover rule (25) is to return control to the pilot in case the aircraft has remained a time T inside the yaw rate envelope deemed admissible and if the pilot's intention indicates a desire toward guiding the aircraft to the inside of the envelope. Note that an appropriate tuning of the dynamic yaw rate threshold (23) and the handover rule (25) is important for a smooth interaction of the assistance system with the pilot. During pilot-in-the-loop experiments, it has been found that pilots preferred short interventions returning the aircraft to the admissible yaw rate envelope. As such, the threshold $\dot{\psi}_{\mathrm{th}}$ and the persistence time T should not be chosen too conservatively, since long interventions, even if safe from the yaw rate excursion point of view, degrade the handling qualities in the pilots' opinions.

C. Lateral Controller Module

The lateral controller module receives the reference $\overline{\dot{\psi}}$ and, in case $\delta_{\mathrm{LAS}} = 1$, generates a virtual input $\tau \in \mathbb{R}$ to be injected into the aircraft. The virtual input τ is calculated using a dynamic inversion approach using the dynamics derived in Section III to obtain a pure integrator relationship. As such, the control law is computed as follows:

$$\tau = \begin{cases} -A_e^{21}\beta - A_e^{22}\dot{\psi} + \nu_e, \\ \qquad \text{if } HS_{\mathrm{SCU}} = 1 \\ -A_d^{21}\beta - A_d^{22}\dot{\psi} - A_d^{23}\hat{\delta}_f - A_d^{24}\hat{\dot{\delta}}_f + \nu_d, \\ \qquad \text{if } HS_{\mathrm{SCU}} = 0 \end{cases} \tag{26}$$

where ν_e and ν_d are the residual controls that need to be designed, whereas $\hat{\delta}_f$ and $\hat{\dot{\delta}}_f$ are estimations of the steering states due to the unavailability of the associated measurement during an SCU failure. Both ν_e and ν_d are calculated as the output of a dedicated proportional-integral (PI) controller that operates on the error signal $\overline{\dot{\psi}} - \dot{\psi}$. The parameters of the PI controllers in each disengaged mode are scheduled in the ground speed v_g and have been tuned to achieve a bandwidth of around 1 Hz and a phase margin of 60° in the aircraft's operational envelope. Note that the tuning was conducted after fixing the control allocator module, as the allocator's algorithm can couple with the imperfect cancellation given by the dynamic inversion controller. Note furthermore that an antiwindup mechanism complements the PI controller structure and uses a tracking mode to achieve bumpless transfer when the signals δ_{LAS} or $\mathrm{HS}_{\mathrm{SCU}}$ change state [31].

As described in Section II-C, in the case in which the SCU is in a failure condition, the steering angle δ_f cannot be directly imposed and becomes unmeasurable. As such, its free castering dynamics become a disturbance that needs to be compensated for. The dynamic inversion law in (26) in the case $\mathrm{HS}_{\mathrm{SCU}} = 0$ accounts for this disturbance, but the signals associated with the SCU need to be estimated. The computation of signals $\hat{\delta}_f$ and $\hat{\dot{\delta}}_f$ is achieved by an extended Kalman filter designed on the dynamics expressed in (20). Namely, the estimator has the form

$$\dot{\hat{x}}_d = A_d\hat{x}_d + B_d\left[\Delta P_b \quad \delta_{\mathrm{rud}}\right]^T + K_d\left(y_d - C_d\hat{x}_d\right) \tag{27}$$

where $\hat{x}_d = [\hat{\beta} \quad \hat{\dot{\psi}} \quad \hat{\delta}_f \quad \hat{\dot{\delta}}_f]^T$, $y_d = [\beta \quad \dot{\psi}]^T$, $C_d = [1 \quad 0 \quad 0 \quad 0; 0 \quad 1 \quad 0 \quad 0]$, and K_d is the Kalman filter gain. The associated process noise covariance matrix Q_d and measurement noise covariance matrix R_d that determine K_d have been selected as diagonal matrices and tuned to achieve satisfactory tracking of the steering states.

D. Control Allocator Module

The control allocator module receives the virtual input request τ, and if $\delta_{\mathrm{LAS}} = 1$, it aims to solve the problem

$$\tau = \begin{cases} \mathbf{B}_e u_e, & \text{if } HS_{\mathrm{SCU}} = 1 \\ \mathbf{B}_d u_d, & \text{if } HS_{\mathrm{SCU}} = 0 \end{cases} \tag{28}$$

where $u_e = [\Delta P_b \quad \delta_f \quad \delta_{\mathrm{rud}}]^T$ and $u_d = [\Delta P_b \quad \delta_{\mathrm{rud}}]^T$, whereas $\mathbf{B}_e$ and $\mathbf{B}_d$ are the second rows of matrices B_e and B_d, respectively. The objective of the allocator is to use the available actuators to efficiently realize the requested virtual input within their constraints. Moreover, the allocator should cope with the actuator failures described in Section II-C by appropriately handling the health status indication signals.

To solve (28), we first note that the yaw rate tracking controller's bandwidth has been kept deliberately slower than the bandwidth of the ground handling actuators so that the problem is framed in terms of the actuator commands, which is a standard assumption as described in [32]. Therefore, we simplify the problem and solve instead

$$\tau = \begin{cases} \mathbf{B}_e u_e^{\mathrm{comm}}, & \text{if } HS_{\mathrm{SCU}} = 1 \\ \mathbf{B}_d u_d^{\mathrm{comm}}, & \text{if } HS_{\mathrm{SCU}} = 0 \end{cases} \tag{29}$$

where $u_e^{\mathrm{comm}} = [\Delta P_b^{\mathrm{all}} \quad \delta_f^{\mathrm{comm}} \quad \delta_{\mathrm{rud}}^{\mathrm{comm}}]^T$, and $u_d^{\mathrm{comm}} = [\Delta P_b^{\mathrm{all}} \quad \delta_{\mathrm{rud}}^{\mathrm{comm}}]^T$. Next, in case $\mathrm{HS}_{\mathrm{SCU}} = 1$, the rate limit constraints on the steering can be reframed as dynamic position limits of the form

$$\begin{aligned} \underline{\delta_f}(t) &= \max\left(-\delta_f^{\max}, \delta_f(t - \Delta T) - \Delta T \dot{\delta}_f^{\max}\right) \\ \overline{\delta_f}(t) &= \min\left(\delta_f^{\max}, \delta_f(t - \Delta T) + \Delta T \dot{\delta}_f^{\max}\right) \end{aligned} \tag{30}$$

where ΔT is the sampling time of the LAS, $\delta_f(t - \Delta T)$ is the steering angle at the previous sampling instant, whereas $\underline{\delta_f}(t)$ and $\overline{\delta_f}(t)$ are the final position limits at time t. We then collect the command saturation constraints in vectors $u_e^{\max}(t) = [P_b^{\max} \quad \overline{\delta_f}(t) \quad \delta_{\mathrm{rud}}^{\max}]^T$, $u_e^{\min}(t) = [-P_b^{\max} \quad \underline{\delta_f}(t) \quad -\delta_{\mathrm{rud}}^{\max}]^T$, $u_d^{\max} = [P_b^{\max} \quad \delta_{\mathrm{rud}}^{\max}]^T$, and $u_d^{\min} = -u_d^{\max}$.

With the previous definitions in place, the allocation algorithm chosen to distribute the commands is a weighted least squares (WLSs) algorithm, which yielded the best results out of the alternatives shown in [22], and which solves

$$u_{e/d}^{\mathrm{comm}}(t) = *\mathrm{argmin}_{\substack{u_{e/d}^{\min}(t) \le u_{e/d}^{\mathrm{comm}}(t) \\ u_{e/d}^{\mathrm{comm}}(t) \le u_{e/d}^{\max}(t)}} \left|\left|\mathbf{B}_{e/d} u_{e/d}^{\mathrm{comm}}(t) - \tau(t)\right|\right|_2^2$$

$$+\gamma^{\text{all}}\left|\left|W_{e/d}^{-1/2}u_{e/d}^{\text{comm}}(t)\right|\right|_2^2 \tag{31}$$

where $W_e \in \mathbb{R}^{3\times 3}$ and $W_d \in \mathbb{R}^{2\times 2}$ are weighting matrices, whereas $\gamma^{\text{all}} > 0$ is a scalar weighting the importance of virtual error mismatch against control effort minimization. The weighting matrices are chosen as diagonal matrices with entries proportional to the squared position limits of the actuators. Higher weights are placed on the entry penalizing the usage of the differential braking command, since usage of the brakes to solve the lateral instability can produce interferences with the AS system. Note that two instances of the problem are compactly expressed in (31), namely, the engaged steering and the disengaged steering modes. Both instances can be treated conceptually in the same manner, since the number of control inputs in vectors u_e or u_d exceeds the dimensionality of the virtual input τ, which is a scalar variable, leading to an overactuated system in both cases. As such, the control effectiveness matrices and the weighting matrices are appropriately assigned in each problem instance and solved similarly. To deal with a BCU failure, during the time in which $\text{HS}_{\text{BCU}} = 0$, the value $P_b^{\max}$ is set to 0 so that the allocator is forced to rely on other actuators to achieve the virtual input τ. Analogously, to deal with an RCU failure starting at time t_{jam} producing a rudder jamming, the associated constraint is tightened as $\delta_{\text{rud}}^{\max} = \delta_{\text{rud}}(t_{\text{jam}})$. Finally, after posing (31), the WLS solver from [33] is exploited to solve the problem and calculate vector $u_{e/d}^{\text{comm}}$, whose entries are passed to the following blocks.

E. Pressure Allocation Module

This module aims to generate appropriate control commands P_{comm}^R and P_{comm}^L to achieve the differential pressure requests from the allocator ΔP_b^{all}, minimizing the interaction with the AS system, and trying to sacrifice as little longitudinal braking performance as possible. The need for a dedicated algorithm arises from the possibility that $\Delta P_b^{\text{all}} \neq \Delta P_{\text{comm}}$ due to the AS algorithm's intervention as explained in Section II-B. The proposed architecture to achieve the previous objectives is presented in Fig. 9. Its main blocks are described next.

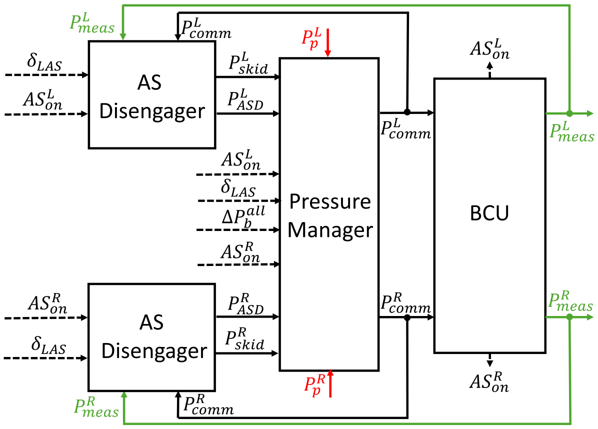

Fig. 9. Pressure Allocation Module architecture. The signals in red are the requests to the ground handling actuators coming from the pilot. The signals in green are measurements from the aircraft. The signals in black are internal.

1) AS Disengager: This block monitors the AS's activation status, indicated by signal $\text{AS}_{\text{on}}^{R/L}$. If $\delta_{\text{LAS}} = 1$, its objective is to maintain $\text{AS}_{\text{on}}^{R/L} = 0$ so that the pressure manager is free to distribute the pressure commands. In case an AS intervention is detected on some side of the MLG at time $t_{\text{on}}^{R/L}$, the AS disengager emits a pressure release command $P_{\text{ASD}}^{R/L}$ of the form

$$P_{\text{ASD}}^{R/L}(t) = P_{\text{meas}}^{R/L}\left(t_{\text{on}}^{R/L}\right) - \alpha_{\text{ASD}}\left(t - t_{\text{on}}^{R/L}\right)$$
$$t \in \left[t_{\text{on}}^{R/L}, t_{\text{off}}^{R/L}\right] \tag{32}$$

where $t_{\text{off}}^{R/L}$ is the time at which the AS becomes inactive, whereas $\alpha_{\text{ASD}} > 0$ is a slope acting as a parameter of the algorithm. The rationale behind (32) is that a general-purpose AS system is guaranteed to eventually become inactive by applying a pressure release of such a form, regaining authority over the brakes. Moreover, the value $P_{\text{skid}}^{R/L}$ is chosen as $P_{\text{skid}}^{R/L} = P_{\text{meas}}^{R/L}(t_{\text{off}}^{R/L})$, which is an estimation of the runway's skid pressure. In practice, it is convenient to choose $t_{\text{off}}^{R/L}$ slightly delayed with respect to the instant in which $\text{AS}_{\text{on}}^{R/L} = 0$ to avoid operating at the limit of the AS's activation. If instead $\delta_{\text{LAS}} = 0$, the AS disengager returns $P_{\text{ASD}}^{R/L} = P_{\text{comm}}^{R/L}$, which acts as a memory of the last commanded value and becomes useful for the following block.

2) Pressure Manager: The pressure manager's goal is to manage the interaction between the pressure requests coming from the pilot, the control allocator, and the AS disengager. To mitigate the coupling with the longitudinal dynamics and prevent the pilot from feeling a stronger deceleration than the one commanded due to interventions of the LAS, the pilot's requests P_p^L and P_p^R dynamically set the maximum budget for ΔP_{comm}. This means that even if $\delta_{\text{LAS}} = 1$, $\Delta P_{\text{comm}} \in [-P_p^R, P_p^L]$ at all times. Moreover, this module should aim to keep the mean deceleration level, i.e., $(P_{\text{meas}}^R + P_{\text{meas}}^L)/2$, as close as possible to the one requested by the pilot so that a smooth lateral correction is injected that does not compromise the longitudinal braking performance, but without triggering the AS system which would be counterproductive. Therefore, the operation limits of the module are determined by both the pilot's commands and the skid pressures $P_{\text{skid}}^{R/L}$.

The challenges previously described are tackled by Algorithm 1. In Algorithm 1, lines 1–3 pass the pilot commands to the BCU in case no correction is needed. Lines 5–7 force the disengagement of the AS by applying the strategy described in (32) on the side (or sides) on which the AS is active. Lines 9–11 compute the operational limits of the algorithm. Note that $P_{\max}^{R/L}$ are auxiliary variables that ensure the commanded pressures are bounded by both the pilot's commands and the last known skid pressure. These variables are used to saturate ΔP_b^{all} to the set of reachable differential pressures. Lines 12–18 allocate the pressures to satisfy ΔP_b^{all} and simultaneously maximize the mean pressure achievable in case $\Delta P_b^{\text{all}} \geq 0$. Lines 13 and 14 try to distribute the pressures by reducing P_{comm}^R with respect to P_{comm}^L, which is chosen as the maximum possible value. In case $P_{\max}^R$ becomes an active constraint in line 14, line 15 will detect a pressure overflow, and instead, the pressure distribution will be conducted by setting P_{comm}^R to $P_{\max}^R$ and increasing P_{comm}^L with respect to

Algorithm 1 Pressure Manager

```
Input:  Pressures $P_p^R$, $P_p^L$, $P_{ASD}^R$, $P_{ASD}^L$, $P_{skid}^R$, $P_{skid}^L$, $\Delta P_b^{all}$
        Binary variables $\delta_{LAS}$, $AS_{on}^R$, $AS_{on}^L$
Output: Pressures $P_{comm}^R$, $P_{comm}^L$
 1: if $\delta_{LAS} == 0$ then                    ▷ No correction needed to pilot's commands
 2:     $P_{comm}^R \leftarrow P_p^R$
 3:     $P_{comm}^L \leftarrow P_p^L$
 4: else                                            ▷ Correction needed to pilot's commands
 5:     if $AS_{on}^R = 1$ or $AS_{on}^L = 1$ then       ▷ Disengage the Anti-skid
 6:         $P_{comm}^R \leftarrow P_{ASD}^R$
 7:         $P_{comm}^L \leftarrow P_{ASD}^L$
 8:     else                                  ▷ Distribute pressures to achieve $\Delta P_b^{all}$
 9:         $P_{max}^R \leftarrow min(P_p^R, P_{skid}^R)$
10:         $P_{max}^L \leftarrow min(P_p^L, P_{skid}^L)$
11:         $\Delta P_b^{all} \leftarrow min(max(\Delta P_b^{all}, -P_{max}^R), P_{max}^L)$
12:         if $\Delta P_b^{all} \geq 0$ then
13:             $P_{comm}^L \leftarrow P_{max}^L$
14:             $P_{comm}^R \leftarrow max(min(P_{comm}^L - |\Delta P_b^{all}|, P_{max}^R), 0)$
15:             if $P_{comm}^L - P_{comm}^R > |\Delta P_b^{all}|$ then
16:                 $P_{comm}^R \leftarrow P_{max}^R$
17:                 $P_{comm}^L \leftarrow min(P_{max}^R + |\Delta P_b^{all}|, P_{max}^L)$
18:             end if
19:         else
20:             $P_{comm}^R \leftarrow P_{max}^R$
21:             $P_{comm}^L \leftarrow max(min(P_{comm}^R - |\Delta P_b^{all}|, P_{max}^L), 0)$
22:             if $P_{comm}^R - P_{comm}^L > |\Delta P_b^{all}|$ then
23:                 $P_{comm}^L \leftarrow P_{max}^L$
24:                 $P_{comm}^R \leftarrow min(P_{max}^L + |\Delta P_b^{all}|, P_{max}^R)$
25:             end if
26:         end if
27:     end if
28: end if
```

P_{comm}^R, guaranteeing the realization of $\Delta P_b^{\mathrm{all}}$ and satisfying all constraints. Finally, lines 19–25 are analogous to lines 12–18 for the case $\Delta P_b^{\mathrm{all}} < 0$.

Remark 2: We have found that the tuning process of the control system can be done systematically with a bottom-up approach. As a first step, we recommend tuning the control allocator and pressure allocation logic to achieve satisfactory performance in terms of virtual input realization, constraint satisfaction, and relative actuator usage. Note that the modularity of the control system allows for including other moment-generating actuators, such as additional control surfaces or differential thrust, if available. Then, we recommend tuning the lateral controller to successfully track yaw rate commands, taking into account the bandwidth recommendations from Sections IV-C and IV-D. Finally, we recommend tuning the supervisor module alongside the pilots expected to operate the target aircraft, due to the importance of a smooth pilot–vehicle interaction.

V. PILOT-IN-THE-LOOP EVALUATION OF THE PROPOSED CONTROL SYSTEM

This section evaluates the proposed assistance system in various scenarios in a pilot-in-the-loop simulation environment. For this purpose, a virtual twin of an aircraft with the studied characteristics has been constructed in a MATLAB/Simulink simulation framework. The aircraft geometry and kinematics, shown in Fig. 1, have been implemented through the Simscape Multibody library [34]. The simulator considers effects such as nonlinear tire dynamics, aerodynamics, landing gear elasticity, track variability, as well as customizable runway friction and aircraft inertial characteristics. The simulator has already been presented and described in detail in [15], where validation was conducted using experimental data from an industrial partner during various types of ground handling maneuvers that excited both the longitudinal and lateral dynamics.

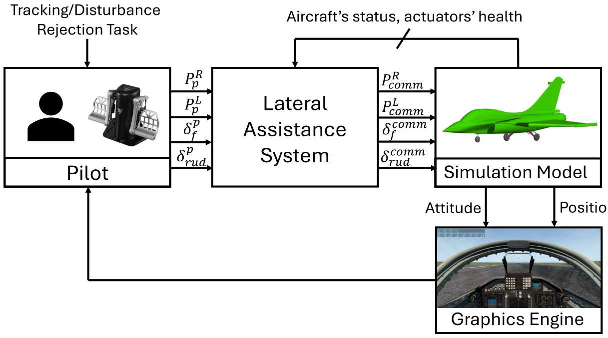

Fig. 10. Pilot-in-the-loop evaluation of the LAS. The pilot aims to achieve the assigned task while the assistance system actively monitors and adjusts the pilot's commands.

The simulation setup is shown in Fig. 10. To achieve a strong immersion level, the user applies the commands P_p^L, P_p^R, δ_{rud}^p, and δ_f^p through a set of rudder pedals (thrustmaster pendular rudder pedals) that resembles the ones from the target aircraft's cockpit. Moreover, a realistic depiction of the scene and the pilot's cockpit is achieved by using the graphics engine provided by the X-Plane 11 simulator. The communication between the graphics engine and the Simulink model is handled by the transmission of UDP packets managed by the XPlane Communication Toolbox [35]. The simulator runs in real time at 1 ms per sampling time with a 33% CPU headroom between samples, considering the MATLAB overhead.

A. Evaluation Scenarios

A set of three challenging scenarios is proposed to evaluate the LAS's ability to aid the pilot in controlling the aircraft's direction during anomalous conditions. A general depiction of the scenarios is shown in Fig. 11, with their corresponding parameters being indicated in Table I. A brief overview of each scenario follows.

1) *Task 1:* This scenario corresponds to a centerline holding task, in which the aircraft starts aligned with the runway centerline. The objective is to brake as fast as possible by minimizing the braking distance while simultaneously trying to deviate from the centerline as little as possible. Starting from $x_{\min}$ and lasting until $x_{\max}$, half of the runway is wet while the other half is dry, implemented by using the friction curves shown in Fig. 3. Moreover, the BCU suffers a failure during the high-speed portion of the maneuver, starting 1.5 s after the beginning of the maneuver and lasting for 2 s while the backup BCU starts up.
2) *Task 2:* This scenario corresponds to a centerline capture task, in which the aircraft starts with a lateral offset with respect to the runway centerline. The objective is to brake as fast as possible by minimizing the braking distance while capturing the centerline and minimizing

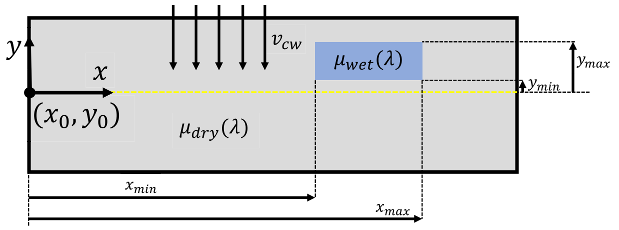

Fig. 11. Graphical representation of the parameters involved in the proposed ground handling evaluation scenarios.

TABLE I

Parameters of the Proposed Evaluation Scenarios

Scenario Code	**Maneuver Type**	**Initial Position** $[m]$ (x_0, y_0)	**Actuator Failure**	**Crosswind** $[km/h]$ v_{cw}	**μ-split Range** $[m]$ (x_{min}, x_{max}) (y_{min}, y_{max})
Task 1	Centerline Holding	(0,0)	BCU	0	(200,500) (0,20)
Task 2	Centerline Capture	(0,10)	SCU	0	(200,500) (2,5)
Task 3	Centerline Capture	(0,10)	RCU	55	Not Applicable

lateral deviations. Pilots were instructed to attempt the centerline capture from the beginning of the experiment and complete the capture within 10 s. Along the path, a wet rectangular patch bounded by vertices $(x_{\text{min}}, y_{\text{min}})$ and $(x_{\text{max}}, y_{\text{max}})$ injects a lateral disturbance that the pilot needs to account for. Additionally, the SCU suffers a failure starting at 1.5 s after the beginning of the maneuver and lasting until its end, transitioning to a disengaged steering configuration, as explained in Section III-B.

3) *Task 3:* This scenario is of the same nature as Task 2. The difference is that the lateral disturbance comprises a constant crosswind of 55 km/h. Moreover, the RCU suffers a failure starting at 1.5 s after the beginning of the maneuver and lasting until its end, jamming the rudder in the process.

The impact of the LAS's presence is evaluated on the previous scenarios by computing key performance metrics. In particular, the average lateral deviation from the centerline e_{avg} is computed to quantify the quality of the lateral tracking task. To evaluate the degree of control over the aircraft's directionality, the maximum attained yaw rate $\dot{\psi}_{\text{max}}$ and side-slip angle β_{max}, as well as their average values $\dot{\psi}_{\text{avg}}$ and β_{avg} are computed. The braking distance d_{br}, computed as the path length traversed by the aircraft from the moment the pilot starts braking, is also computed. Finally, to evaluate the performance of the EKF proposed in Section IV-C to deal with the unavailability of the SCU signals during its failure, we compute the normalized mean absolute error (NMAE) of the estimator's performance, denoted as $\hat{\delta}^e_f$ and $\hat{\dot{\delta}}^e_f$ for the steering angle and steering angle rate, respectively. For each experiment, the NMAE is normalized by the range of the ground truth data in such an experiment to make the estimation errors comparable between runs, as different excursions of the SCU signals can be obtained depending on the pilot's behavior. For all scenarios, an aircraft configuration of $m = 3500$ kg with an initial speed of 200 km/h is considered.

TABLE II

Average Performance Metrics Over Tasks 1–3. L.A.S. Stands for Lateral Assistance System. N/A Stands for Not Applicable

Scenario	$\dot{\psi}_{max}$ $[deg/s]$	$\dot{\psi}_{avg}$ $[deg/s]$	β_{max} $[deg]$	β_{avg} $[deg]$	e_{avg} $[m]$	d_{br} $[m]$	$\hat{\delta}^e_f$ $[\%]$	$\hat{\dot{\delta}}^e_f$ $[\%]$
Task 1 L.A.S. Off	17.9	5.1	6.3	1.8	3.4	403.4	N/A	N/A
Task 1 L.A.S. On	10.8	2.7	3.6	1.1	1.7	464.7	N/A	N/A
Task 2 L.A.S. Off	26.3	7.5	9.8	2.8	6.8	364.3	N/A	N/A
Task 2 L.A.S. On	15.1	4.1	4.6	1.6	5.3	438.2	5.3	9.6
Task 3 L.A.S. Off	21.0	6.7	9.7	2.8	5.9	286.3	N/A	N/A
Task 3 L.A.S. On	10.8	4.0	6.3	2.3	5.5	386.4	N/A	N/A

B. Results

The three scenarios described in Section V-A were evaluated by conducting experiments with volunteers acting as pilots, instructed to accomplish the tasks. The experiments were designed following [36], which provides guidelines for aspects such as the number of evaluation pilots, the suitability of blind evaluations, or the evaluation time. Five pilots, denoted as Pilots A–E, operated the simulation environment by executing several repetitions of Tasks 1–3, both with the LAS active and inactive. The five pilots who evaluated the system's performance were student pilots working toward their general aviation licenses. Three repetitions were performed per configuration, totaling 90 experiments. Before every experiment, each pilot was briefed on the task to be accomplished and the anomalies they would face, but the usage of the LAS was not revealed to avoid biasing their performance. Note that, as indicated in [36], a small sample of pilots under repeated evaluations, such as the one proposed in this study, is appropriate since the consistency of obtained data is deemed higher than in evaluations with a larger cohort of pilots but with fewer experiments per pilot.

Table II shows the average performance metrics over the three proposed scenarios. All lateral performance metrics improved by using the assistance system. The greatest improvements in lateral deviation minimization were observed in Tasks 1 and 2, while mild improvements were observed in Task 3. As indicated by the yaw rate and side-slip metrics, the aircraft was more predictable from a directional point of view, as confirmed by the pilots' opinions as well. The improvement in directional performance came at the expense of braking distance, which was expected due to the active usage of the differential braking correction. The mild improvements in Task 3 are attributed to the fact that after the failure of the RCU, the aircraft dynamics do not suffer additional sudden variations, as the crosswind is kept constant throughout the maneuver. This situation gives time to the pilots to adapt and adjust their behavior to cope with the proposed scenario. In contrast, both Task 1 and Task 2 expose the pilots to sudden variations in the runway's grip after the respective actuator's failure. This difference in performance improvement

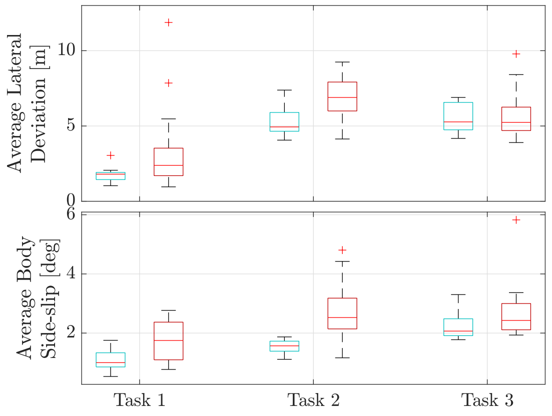

Fig. 12. Distribution of the performance metrics disaggregated by task (Tasks 1, 2, and 3). In green: lateral assistance active. In red: lateral assistance inactive. Average lateral deviation e_{avg} (top). Average body side-slip β_{avg} (bottom).

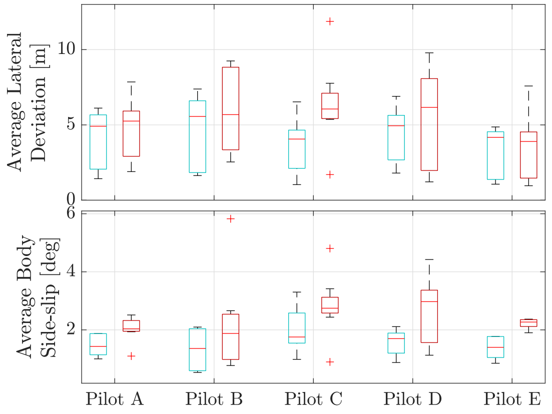

Fig. 13. Distribution of the performance metrics in Tasks 1–3 disaggregated by pilot. In green: lateral assistance active. In red: lateral assistance inactive. Average lateral deviation e_{avg} (top). Average body side-slip β_{avg} (bottom).

between tasks highlights the role of the assistance system in dealing with sudden, unexpected dynamical changes. Fig. 12 shows the distribution of the average lateral deviation e_{avg} and average side-slip angle β_{avg} disaggregated by task. Outliers are indicated as red crosses with a detection threshold of 1.5× the interquartile range. The variability of the metrics was reduced for all tasks, and a significant reduction was obtained for Tasks 1 and 2.

To account for the interpilot variability, Fig. 13 shows the distribution of the same performance metrics for Pilots A–E. It can be seen that a skill level difference indeed exists. Nonetheless, all pilots benefited from the presence of the LAS in terms of directional stability.

To generate insight into the algorithm's inner workings, the detailed results of two experiments conducted by Pilot D will be shown. Both concern Task 2, which suffers from the critical disengaged steering dynamics due to a failure in the SCU. In the first case, the LAS was inactive. The resulting aircraft's trajectory and evolution of the yaw rate $\dot{\psi}$ are shown in Fig. 14. Note that the longitudinal and lateral displacements indicate the position of the aircraft's CoG along the runway's reference frame (x, y) as indicated in Fig. 11 with the initial condition of the experiment as stated in Table I.

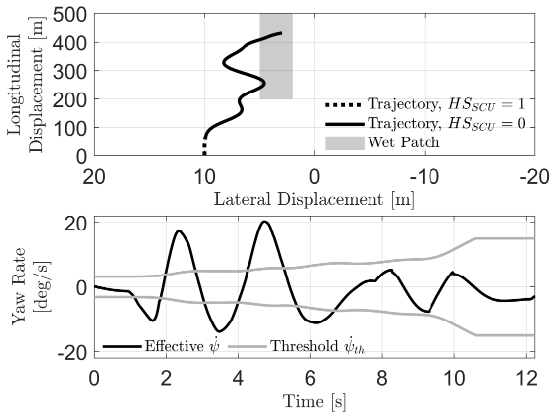

Fig. 14. Performance evaluation of Task 2 with the LAS inactive. Trajectory traversed by the aircraft during the portions of healthy (dotted line) and faulty (solid line) SCU operation. The geometrical location of the wet patch is shaded in gray (top). Time evolution of the yaw rate $\dot{\psi}$ and the admissible envelope limit $\dot{\psi}_{\text{th}}$ (bottom).

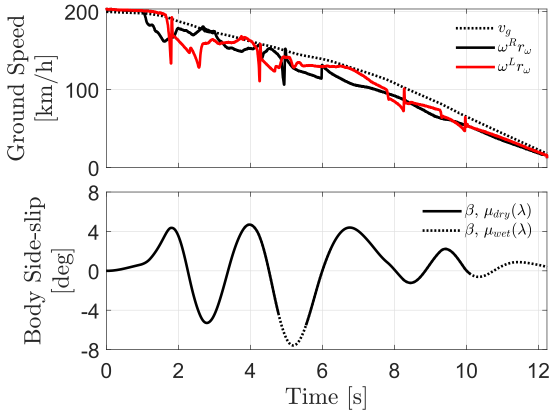

Fig. 15. Time evolution of Task 2 with the LAS inactive. Ground speed v_g and wheel speeds $\omega^{R/L} r_\omega$ (top). Body side-slip β when traversing the dry (solid line) or wet (dotted line) runway sections (bottom).

As noted in the top plot, the pilot shows great difficulties in keeping directionality and cannot capture the centerline once the aircraft hits the wet patch, which is also made more difficult due to the disengaged steering dynamics and the subsequent loss of control authority. The bottom plot indicates that the aircraft reaches dangerous yaw rate values during the high-speed portion of the maneuver, outside the defined safe envelope, indicating that the LAS would have intervened had it been active. Fig. 15 (top) shows instead the evolution of the ground speed v_g together with the linear wheel speeds $\omega^R r_\omega$ and $\omega^L r_\omega$, whereas the bottom plot shows the side-slip angle β.

As can be observed, a strong oscillatory behavior is shown between 2 and 7 s, caused by the steering dynamics and the first contact with the wet patch. The aircraft is brought back under control around the 8-s mark onward.

Fig. 16 shows the aircraft's trajectory and evolution of the yaw rate $\dot{\psi}$ with the LAS active.

As can be noted in the top plot, the pilot manages to stay closer to the centerline and achieves the goal by the end of the maneuver. In the bottom plot, five interventions of the assistance system are observed, corresponding to incipient

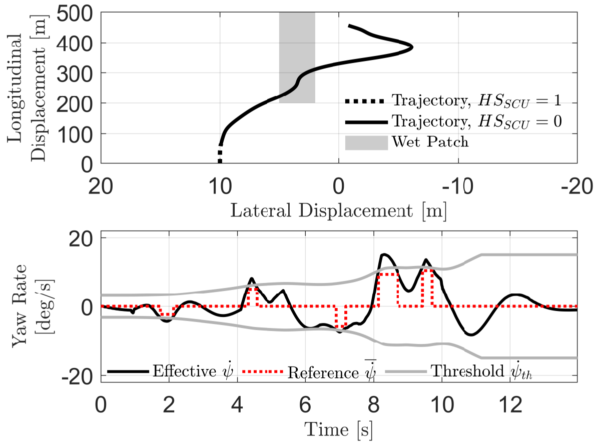

Fig. 16. Performance evaluation of Task 2 with the LAS active. Trajectory traversed by the aircraft during the portions of healthy (dotted line) and faulty (solid line) SCU operation. The geometrical location of the wet patch is shaded in gray (top). Time evolution of the yaw rate $\dot{\psi}$, its reference $\bar{\dot{\psi}}$, and the admissible envelope limit $\dot{\psi}_{\text{th}}$ (bottom).

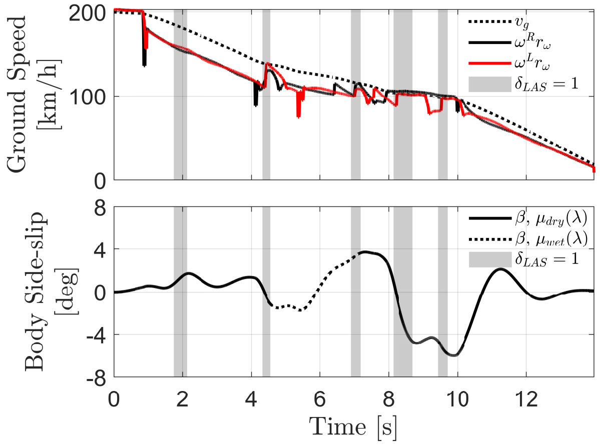

Fig. 17. Time evolution of Task 2 with the LAS active. Ground speed v_g and wheel speeds $\omega^{R/L} r_\omega$ (top). Body side-slip β when traversing the dry (solid line) or wet (dotted line) runway sections (bottom). The intervention instants of the LAS are shaded in gray.

excursions from the safety envelope, which are evidenced by the non-null yaw rate reference $\bar{\dot{\psi}}$. The assistance system is able to bring the aircraft back under the pilot's control quickly. In Fig. 17, the evolution of the ground speed and side slip is shown, together with the instants in which the LAS actively intervened, shaded in gray.

As observed, the main excitation of the lateral dynamics is associated with the transition between the wet and dry runway, which is counteracted by the assistance system. Fig. 18 shows the performance of the controller in terms of control allocation instead.

The top plot shows the requested virtual input correction τ during the intervention instants against the effective value obtained τ_{eff}, which is computed as $\mathbf{B}_d u_d$, according to (28). The difference between τ and τ_{eff} is explained by the actuator dynamics, which were neglected to pose the problem as in (29). Nevertheless, the correction is achieved after the initial transient, which is effective in correcting the lateral instability. The bottom plot shows instead the differential braking request ΔP_b^{all} that the allocator returns, together with the effective differential braking attained ΔP_b and the status of the AS $\text{AS}_{\text{on}}^{R/L}$. It can be observed that the first intervention does not call for differential braking usage, as the rudder is still effective during high speeds. From the second intervention on, each time the differential braking is requested, the AS is quickly disengaged to achieve the desired request ΔP_b^{all}. The fourth and fifth interventions are subject to a transient constraint imposed by the pilot releasing the right pedal, as evidenced by the shaded gray area between 8 and 10 s. It can be seen that Algorithm 1 effectively prevents ΔP_b from crossing to the forbidden area and achieves the closest possible differential pressure to the requested one.

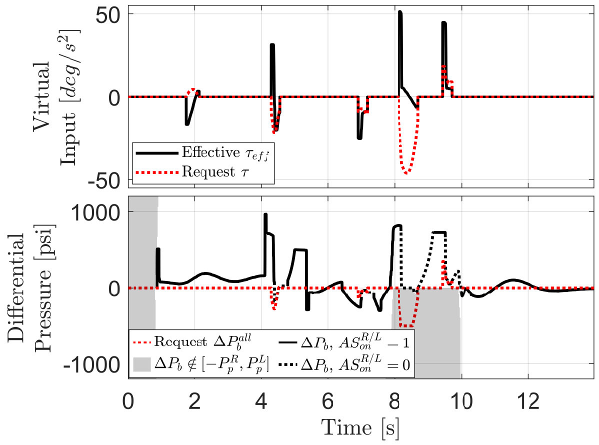

Fig. 18. Performance evaluation of the allocation modules in Task 2 with the LAS active. Comparison between the requested virtual input τ and its effective value τ_{eff} (top). Comparison between the requested differential pressure ΔP_b^{all} (dotted red line) and its effective value attained during active AS intervention (solid black line) and during no AS intervention (dotted black line) (bottom). The unreachable values of differential pressure are shaded in gray.

C. Performance Under Parameter Variability

To analyze the robustness of the proposed LAS to aircraft parameter variations, an additional batch of pilot-in-the-loop experiments was conducted with the same pilots A-E. Since Task 2 was considered by the pilots to be the most challenging scenario proposed, three additional variants to this task were explored, denoted as Task 2-A, Task 2-B, and Task 2-C. The tasks' objectives were the same as Task 2 described in Section V-A, and the anomalies faced were the same ones as in Task 2 described in Table I. However, the aircraft parameters were altered as described in Table III. The proposed parameter variations enable us to examine the LAS's performance across the aircraft's operational envelope. Three repetitions were conducted per configuration, with and without the LAS active, for a total of 90 experiments. The results are presented in Table IV, which shows the average performance metrics over the three Task 2 variants. The results confirm the system's ability to assist the pilot in mitigating the directional excursions even in non-nominal aircraft configurations. Fig. 19 shows the distribution of the average lateral deviation e_{avg} and average side-slip angle β_{avg} disaggregated by task. Tasks 2-A and 2-C caused the most directional difficulties when the assistance system was not employed, as demonstrated by the side slip, yaw rate, and lateral deviation metrics. This is consistent

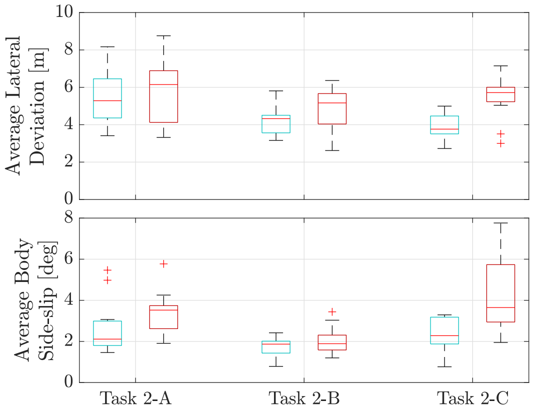

Fig. 19. Distribution of the performance metrics disaggregated by task (Tasks 2-A, 2-B, and 2-C). In green: lateral assistance active. In red: lateral assistance inactive. Average lateral deviation e_{avg} (top). Average body side-slip β_{avg} (bottom).

TABLE III

AIRCRAFT PARAMETERS FOR TASKS 2-A, 2-B, AND 2-C

Scenario Code	Mass $[kg]$	CoG Position	MLG Tire Condition
Task 2-A	4000	Aft	Nominal
Task 2-B	3000	Forward	Nominal
Task 2-C	3500	Nominal	Worn out

TABLE IV

AVERAGE PERFORMANCE METRICS OVER TASKS 2-A, 2-B, AND 2-C. L.A.S. STANDS FOR LATERAL ASSISTANCE SYSTEM. N/A STANDS FOR NOT APPLICABLE

Scenario	$\dot{\psi}_{max}$ $[deg/s]$	$\dot{\psi}_{avg}$ $[deg/s]$	β_{max} $[deg]$	β_{avg} $[deg]$	e_{avg} $[m]$	d_{br} $[m]$	$\hat{\delta}^e_f$ [%]	$\dot{\hat{\delta}}^e_f$ [%]
Task 2-A L.A.S. Off	25.5	7.9	10.9	3.4	5.8	355.2	N/A	N/A
Task 2-A L.A.S. On	16.5	5.2	6.7	2.7	5.4	453.2	8.9	9.5
Task 2-B L.A.S. Off	19.5	6.2	7.3	2.1	4.8	370.1	N/A	N/A
Task 2-B L.A.S. On	12.8	3.9	4.8	1.7	4.2	414.4	5.8	10.0
Task 2-C L.A.S. Off	29.3	10.6	12.0	4.3	5.5	367.4	N/A	N/A
Task 2-C L.A.S. On	14.7	5.1	6.3	2.4	3.9	406.9	7.5	9.1

with the evaluated aircraft configurations, as an aft CoG and a poor cornering stiffness of the worn-out MLG tires are associated with oversteering ground handling characteristics. When the assistance system was employed, less variability in performance between tasks was obtained, highlighting the control system's ability to improve the handling qualities over the aircraft's operational envelope.

The pilots' performance on this batch of experiments is shown in Fig. 20, which shows that the pilots benefited from the presence of the assistance system. In general, lower metrics were attained, and thus, the tasks were completed more effectively.

After each experiment, the pilot's opinions on the ground handling characteristics were evaluated through the Cooper–Harper scale, which quantifies the pilot compensation required to achieve adequate task performance [30], [37]. The scale assigns a score between 1 and 10 depending on the pilot compensation perceived. Higher scores indicate high compensation, while lower scores indicate little compensation required by the pilot. The results are summarized in Table V, where each row represents a set of 15 pilot ratings. The configurations with the assistance system active were preferred by the pilots, who gave lower scores on average than with the assistance system inactive. The previous scores also allow us to confirm the benefits of the control system in terms of handling qualities and pilot–vehicle interaction.

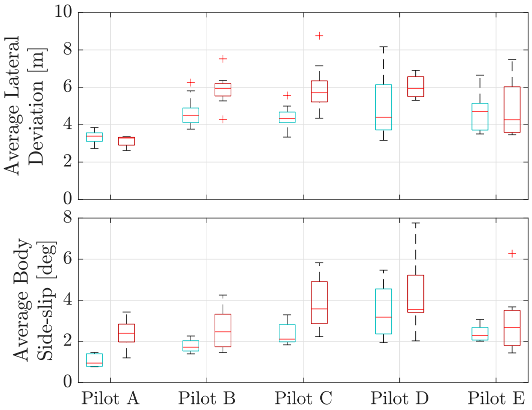

Fig. 20. Distribution of the performance metrics in Tasks 2-A, 2-B, and 2-C disaggregated by pilot. In green: lateral assistance active. In red: lateral assistance inactive. Average lateral deviation e_{avg} (top). Average body side-slip β_{avg} (bottom).

TABLE V

COOPER–HARPER RATINGS OVER TASKS 2-A, 2-B, AND 2-C. L.A.S. STANDS FOR LATERAL ASSISTANCE SYSTEM

Scenario	Median	Minimum	Maximum
Task 2-A L.A.S. Off	5	4	7
Task 2-A L.A.S. On	4	3	6
Task 2-B L.A.S. Off	4	2	7
Task 2-B L.A.S. On	3	1	5
Task 2-C L.A.S. Off	5	2	7
Task 2-C L.A.S. On	3	2	5

VI. CONCLUSION

This article has dealt with designing and evaluating a modular control system dedicated to correcting incipient lateral instabilities during high-speed aircraft rollout for tricycle-type landing gear geometries. The LAS is able to simultaneously use the commonly employed ground handling actuators to improve directional control, namely the differential braking, the rudder, and the nose wheel steering. The control system is robust against failures of different classes in each actuator, and special emphasis was dedicated to smooth interaction with the AS system so that differential braking can be used effectively when required. The control system was evaluated in a pilot-in-the-loop simulation environment, which showed significant improvement in performance in terms of lateral error minimization for centerline capture and centerline holding-type maneuvers with different pilots, anomalous conditions, and aircraft configurations. As future research directions, the practical implementation of the proposed control system is envisioned, together with its evaluation with professional pilots. Moreover, ongoing efforts are being devoted to the problem of designing an architecture able to jointly optimize the longitudinal and lateral performance metrics, capable of smoothly interacting with the pilot.

REFERENCES

[1] International Air Transport Association (IATA). (2023). *IATA Safety Report 2023*. [Online]. Available: https://www.iata.org/en/publications/safety-report/

[2] N. Distefano and S. Leonardi, "Aircraft runway excursion features: A multiple correspondence analysis," *Aircr. Eng. Aerosp. Technol.*, vol. 91, no. 1, pp. 197–203, Jan. 2018, doi: 10.1108/aeat-11-2017-0244.

[3] L. D'Avico, M. Tanelli, S. M. Savaresi, M. Airoldi, and G. Rapicano, "A deceleration-based algorithm for anti-skid control of aircraft," *IFAC-PapersOnLine*, vol. 50, no. 1, pp. 14168–14173, Jul. 2017, doi: 10.1016/j.ifacol.2017.08.2082.

[4] Z. Jiao, Z. Wang, D. Sun, X. Liu, Y. Shang, and S. Wu, "A novel aircraft anti-skid brake control method based on runway maximum friction tracking algorithm," *Aerosp. Sci. Technol.*, vol. 110, Mar. 2021, Art. no. 106482, doi: 10.1016/j.ast.2020.106482.

[5] M. Q. Chen, W. S. Liu, Y. Z. Ma, J. Wang, F. R. Xu, and Y. J. Wang, "Mixed slip-deceleration PID control of aircraft wheel braking system," *IFAC-PapersOnLine*, vol. 51, no. 4, pp. 160–165, 2018, doi: 10.1016/j.ifacol.2018.06.059.

[6] M. Chen, F. Xu, X. Liang, and W. Liu, "MSD-based NMPC aircraft anti-skid brake control method considering runway variation," *IEEE Access*, vol. 9, pp. 51793–51804, 2021, doi: 10.1109/ACCESS.2021.3070066.

[7] N. Bai et al., "An aircraft brake control algorithm with torque compensation based on RBF neural network," *Chin. J. Aeronaut.*, vol. 37, no. 1, pp. 438–450, Jan. 2024, doi: 10.1016/j.cja.2023.06.010.

[8] A. W. Ndiaye, J.-M. Biannic, M. Cassaro, C. Combier, and J.-B. Lestage, "Advanced aircraft braking control laws design and validation," in *Proc. 9th Eur. Conf. Aeronaut. Space Sci. (EUCASS)*, 2021, pp. 1–16, doi: 10.13009/EUCASS2022-4404.

[9] M. Mayolle, S. Pellet, and X. Lesceu, "Lateral runway excursions upon landing," *Saf. 1st*, no. 20, pp. 14–27, Jul. 2015. [Online]. Available: https://safetyfirst.airbus.com/lateral-runway-excursions-upon-landing/

[10] D. Correia and A. Ferreira, "Aircrafts on-ground dynamics models and simulation software: State-of-the-art," *Sustainability*, vol. 13, no. 16, p. 9147, Aug. 2021, doi: 10.3390/su13169147.

[11] D. H. Klyde, T. T. Myers, R. E. Magdaleno, and J. G. Reinsberg, "Identification of the dominant ground handling characteristics of a navy jet trainer," *J. Guid., Control, Dyn.*, vol. 25, no. 3, pp. 546–552, May 2002, doi: 10.2514/2.4915.

[12] D. H. Klyde, T. Myers, A. K. Lampton, M. Draper-Donley, and M. Bishop, "Improved models for the ground handling assessment of navy aircraft," in *Proc. AIAA Atmos. Flight Mech. Conf.*, Jan. 2015, pp. 1–14, doi: 10.2514/6.2015-0241.

[13] K. Georgieva and V. Serbezov, "Mathematical model of aircraft ground dynamics," in *Proc. Int. Conf. Mil. Technol. (ICMT)*, May 2017, pp. 514–519, doi: 10.1109/MILTECHS.2017.7988812.

[14] J. Rankin, B. Krauskopf, M. Lowenberg, and E. Coetzee, "Operational parameter study of aircraft dynamics on the ground," *J. Comput. Nonlinear Dyn.*, vol. 5, no. 2, Apr. 2010, Art. no. 021007, doi: 10.1115/1.4000797.

[15] J. J. Mendoza Lopetegui, G. Papa, M. Morandini, and M. Tanelli, "Shock absorber leakage impact on aircraft lateral stability during ground handling maneuvers," *J. Guid., Control, Dyn.*, vol. 46, no. 6, pp. 1066–1082, Jun. 2023, doi: 10.2514/1.g006933.

[16] B. Chen, Z. Jiao, and S. S. Ge, "Nonlinear control of aircraft on ground runway keeping," in *Proc. Int. Conf. Fluid Power Mechatronics*, Aug. 2011, pp. 576–581, doi: 10.1109/FPM.2011.6045829.

[17] C. Roos, J.-M. Biannic, S. Tarbouriech, C. Prieur, and M. Jeanneau, "On-ground aircraft control design using a parameter-varying anti-windup approach," *Aerosp. Sci. Technol.*, vol. 14, no. 7, pp. 459–471, Oct. 2010, doi: 10.1016/j.ast.2010.02.004.

[18] D. Lemay, Y. Chamaillard, M. Basset, and J. P. Garcia, "Gain-scheduled yaw control for aircraft ground taxiing," *IFAC Proc. Volumes*, vol. 44, no. 1, pp. 12970–12975, Jan. 2011, doi: 10.3182/20110828-6-it-1002.00692.

[19] J. Duprez, F. Mora-Camino, and F. Villaume, "Control of the aircraft-on-ground lateral motion during low speed roll and manoeuvers," in *Proc. IEEE Aerosp. Conf.*, vol. 4, Mar. 2004, pp. 2656–2666, doi: 10.1109/AERO.2004.1368061.

[20] Q. Yin, H. Nie, X. Wei, and M. Zhang, "Aircraft electric anti-skid braking and combined direction control system using co-simulation and experimental methods," *Proc. Inst. Mech. Eng., G, J. Aerosp. Eng.*, vol. 234, no. 2, pp. 173–191, Feb. 2020, doi: 10.1177/0954410019852825.

[21] Y. Dai, J. Song, L. Yu, Z. Lu, S. Zheng, and F. Li, "The lateral control during aircraft-on-ground deceleration phases," *Aerosp. Sci. Technol.*, vol. 95, Dec. 2019, Art. no. 105482, doi: 10.1016/j.ast.2019.105482.

[22] E. Sadien et al., "A simple and efficient control allocation scheme for on-ground aircraft runway centerline tracking," *Control Eng. Pract.*, vol. 95, Feb. 2020, Art. no. 104228, doi: 10.1016/j.conengprac.2019.104228.

[23] E. Sadien et al., "A dynamic multi-axis control allocation scheme for real-time applications," *Int. J. Control*, vol. 97, no. 5, pp. 970–981, May 2024, doi: 10.1080/00207179.2023.2186308.

[24] Y. Dai, L. Yu, J. Song, L. Abi, and S. Zheng, "Aircraft ground braking assistant control based on pilot control model," *IEEE Access*, vol. 8, pp. 88643–88650, 2020, doi: 10.1109/ACCESS.2020.2993173.

[25] D. H. Klyde, J. G. Reinsberg, E. Sanders, and A. Kokolios, "Flight-test evaluation of stability augmentation steering system for aircraft ground handling," *J. Guid., Control, Dyn.*, vol. 27, no. 1, pp. 41–51, Jan. 2004, doi: 10.2514/1.3168.

[26] G. Di Rito, R. Galatolo, and F. Schettini, "Multi-variable aircraft directional control with anti-skid differential brakes," in *Proc. 31st Congr. Int. Council Aeronaut. Sci. (ICAS)*, 2018, pp. 1–9. [Online]. Available: https://www.icas.org/icasarchive/ICAS2018/data/preview/ICAS20180607.htm

[27] J. J. Mendoza Lopetegui, G. Finotto, and M. Tanelli, "Gain-scheduled design of active braking control systems for optimized ground handling in aircraft," in *Proc. Eur. Control Conf. (ECC)*, Jun. 2024, pp. 267–272, doi: 10.23919/ecc64448.2024.10591105.

[28] J. J. Mendoza Lopetegui, G. Papa, M. Morandini, and M. Tanelli, "Data-driven modeling and regulation of aircraft brakes degradation via antiskid controllers," *IEEE Trans. Rel.*, vol. 72, no. 3, pp. 889–899, Sep. 2023, doi: 10.1109/TR.2022.3194646.

[29] E. Fiala, "Seitenkraften am rollenden luftreifen (lateral forces on rolling pneumatic tires)," *Zeitschrift des Vereines Deutscher Ingenieure (V.D.I.) (J. Assoc. German Eng.)*, vol. 96, no. 29, pp. 973–979, 1954.

[30] G. E. Cooper and R. P. Harper, *The Use of Pilot Rating in the Evaluation of Aircraft Handling Qualities*, document NASA TND-5153, 1969. [Online]. Available: https://apps.dtic.mil/sti/pdfs/AD0689722.pdf

[31] K. Åström and T. Hägglund, *Advanced PID Control*. Pittsburgh, PA, USA: ISA–The Instrumentation, Systems and Automation Society, 2006.

[32] T. A. Johansen and T. I. Fossen, "Control allocation—A survey," *Automatica*, vol. 49, no. 5, pp. 1087–1103, May 2013, doi: 10.1016/j.automatica.2013.01.035.

[33] O. Härkegård. (2004). *Quadratic Programming Control Allocation Toolbox (QCAT)*. [Online]. Available: https://www.mathworks.com/matlabcentral/fileexchange/4609-qcat

[34] S. Miller. (2021). *Simscape Multibody Contact Forces Library*. [Online]. Available: https://github.com/mathworks/Simscape-Multibody-Contact-Forces-Library/releases/tag/21.1.5.0

[35] C. Teubert, J. Watkins, and B. Bole. (2020). *X-Plane Communication Toolbox (XPC)*. [Online]. Available: https://software.nasa.gov/software/ARC-17185-1

[36] R. P. Harper and G. E. Cooper, "Handling qualities and pilot evaluation," *J. Guid., Control, Dyn.*, vol. 9, no. 5, pp. 515–529, Sep. 1986, doi: 10.2514/3.20142.

[37] D. G. Mitchell, "Fifty years of the Cooper-Harper scale," in *Proc. AIAA Scitech Forum*, Jan. 2019, pp. 1–18, doi: 10.2514/6.2019-0563.

Open Access funding provided by 'Politecnico di Milano' within the CRUI CARE Agreement